Chapter 3

Overview of the Experiment

The experiment described in this thesis is the first experiment performed at the internal-target facility of NIKHEF. The experimental setup allows the measurement of the $(e, e'p)$ and $(e, e'd)$ reactions for tensor-polarized deuterium. In this chapter an overview of the experiment is given, together with its major design considerations. We give a general discussion of the kinematics, the electron storage ring and the principle of the internal target. In order to optimize the detection system, a Monte Carlo code was written which is briefly described in section 3.2. Furthermore, the results of a study of the spatial distribution of the stored electron beam are presented in section 3.3. In section 3.4 the design considerations for the polarized deuterium target will be discussed. A detailed description of the polarized source, internal target, polarimeters and detection system will be given in the next chapters.

3.1 Description of the Experiment

3.1.1 Planned measurements

The goal of our experiment was to measure the spin-dependent observables for both $^2\overset{\leftrightarrow}{\mathrm{H}}(e, e'd)$ elastic and $^2\overset{\leftrightarrow}{\mathrm{H}}(e, e'p)$ quasi-elastic scattering over a large kinematic range. The general expression of the cross section for polarized deuteron electro-disintegration has the following form [6]:

$$
\sigma = \sigma_0 \Bigg[1 \;\; + \;\; \sqrt{3}\, P_z \, \sin\theta_d \, \sin\phi_d \, iT_{11} + \frac{1}{\sqrt{2}}\, P_{zz} \left(\frac{3\cos^2\theta_d - 1}{2}\, T_{20} \right.
$$
$$
\left. - \sqrt{\frac{3}{2}} \, \sin 2\theta_d \, \cos\phi_d \, T_{21} + \sqrt{\frac{3}{2}} \, \sin^2\theta_d \, \cos 2\phi_d \, T_{22} \right) \Bigg] \, .
\tag{3.1}
$$

Here, σ_0 is the unpolarized cross section, P_z and P_{zz} are the degree of vector and tensor polarization defined as $P_z = n_+ - n_-$ and $P_{zz} = 1 - 3n_0$, where n_+, n_0, and n_- are

the relative populations of the various nuclear spin projections on the direction of the magnetic holding field. The polarization direction of the deuteron is defined by the angles θ_d and ϕ_d in the frame where the z-axis is along the direction of the virtual photon and the y-axis is defined by the vector product of the incoming and outgoing electron momenta. For elastic scattering [3] the general expression of the cross section is as in Eq. 3.1 apart from the iT_{11} term which vanishes under the assumption of time reversal invariance and one-photon exchange. The tensor analyzing powers T_{2j} of the reaction are a direct measure of the spin structure of the deuteron ground state and are particularly sensitive to the D-wave admixture (see chapter 2). Our experiment focused on the tensor analyzing powers T_{2j} for both elastic scattering and quasi-elastic proton knock-out using a 565 MeV electron beam.
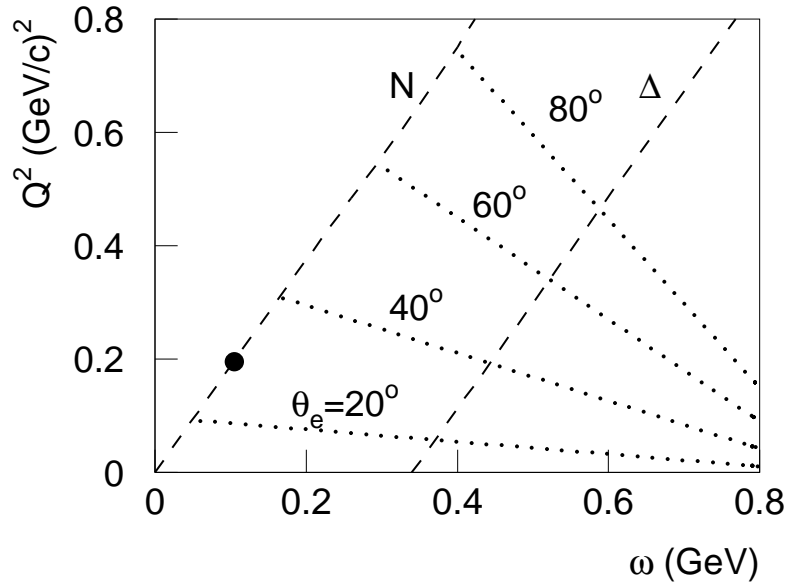

Figure 3.1: *The available phase space for a 565 MeV electron beam. The lines indicate kinematics with constant scattering angle (dotted) and constant missing mass (dashed). The filled circle indicates the average kinematics of the experiment.*

Fig. 3.1 shows the kinematically available phase space in the ω - Q^2 plane for a beam energy of 565 MeV. Lines indicate constant values of scattering angle (dotted) and invariant mass (dashed). The average electron kinematics are indicated as a filled circle.

The small cross sections and the limited available luminosity define requirements for the angular acceptances. The cross section for elastic electron-deuteron scattering ranges from 10^{-6} to 10^{-11} (barn/sr) between $Q^2=0.05$ and 0.6 (GeV/c)^2 [38]. Similarly, the coincidence cross section for the exclusive quasi-elastic $(e, e'p)$ reaction ranges from a few μb/MeV/sr^2 to a few nb/MeV/sr^2 for missing momenta between $p_m= 0$ and 300 (MeV/c) [39]. The angular range of the scattered electron and recoil deuteron is shown
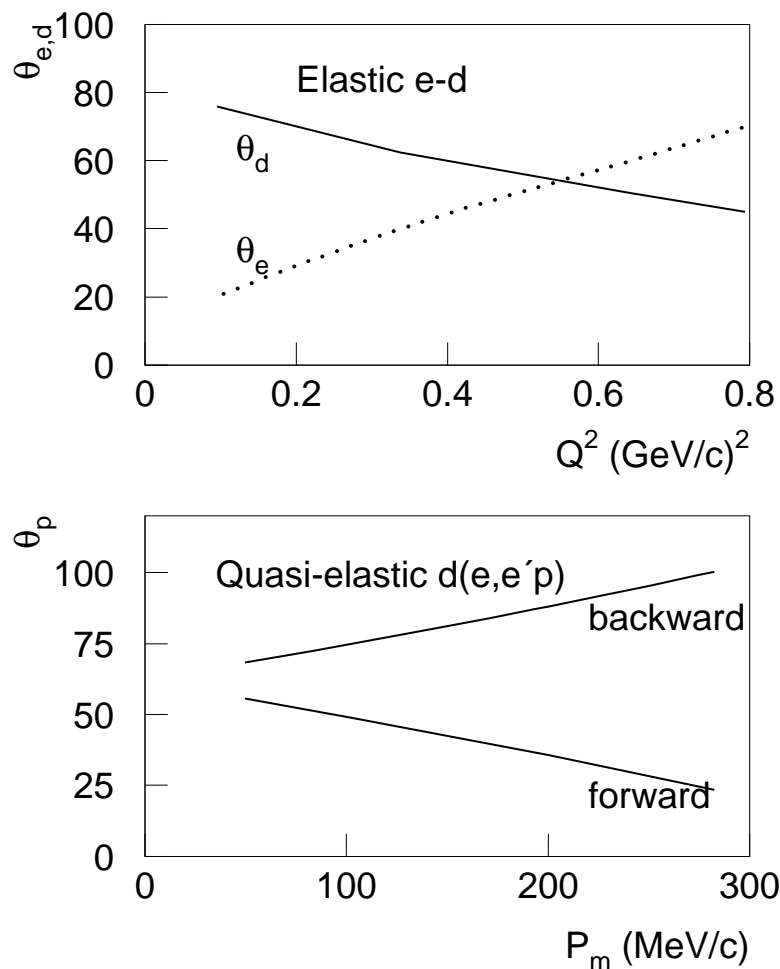
Figure 3.2: *Electron-deuteron elastic scattering angles for a 565 MeV beam (top). Angles of the knock-out proton in quasi-elastic scattering for perpendicular kinematics (bottom).*

in Fig. 3.2 (top) for a beam energy of 565 MeV. The angular span of the knocked-out proton is shown in Fig. 3.2 (bottom) as a function of p_m. In order to obtain significant results within a reasonable amount of beam time, especially at large Q^2 for the elastic channel or at high p_m for the inelastic channel, it is necessary to integrate over large momentum and angular acceptances. In addition, the complete angular range of the experiment should be measured simultaneously, which has the advantage of reducing systematic errors associated with changes in detector angles. Therefore, it is imperative to use large solid angle detectors with acceptances in the order of hundreds of msr.

The present experiment was carried out with a beam current of 80 mA and a target thickness of 2×10^{13} ^{2}H·cm^{-2}. The electron detector had a solid angle of 180 msr $(\Delta\theta \times \Delta\phi = 424 \times 424$ mrad$^2)$ and was positioned at a central scattering angle of

$\theta_e = 30°$. The hadron detector had a 300 msr solid angle and positioned at a central angle of $\theta_{p,d} = 80°$. The average value of the transferred momenta was 0.2 $(GeV/c)^2$, while the missing momenta for the $(e, e'p)$ reactions ranged from 0 - 250 MeV/c. The target spin was oriented in directions parallel ($\theta_d \sim 0°$) and perpendicular to ($\theta_d \sim 90°$) to the transferred momentum.

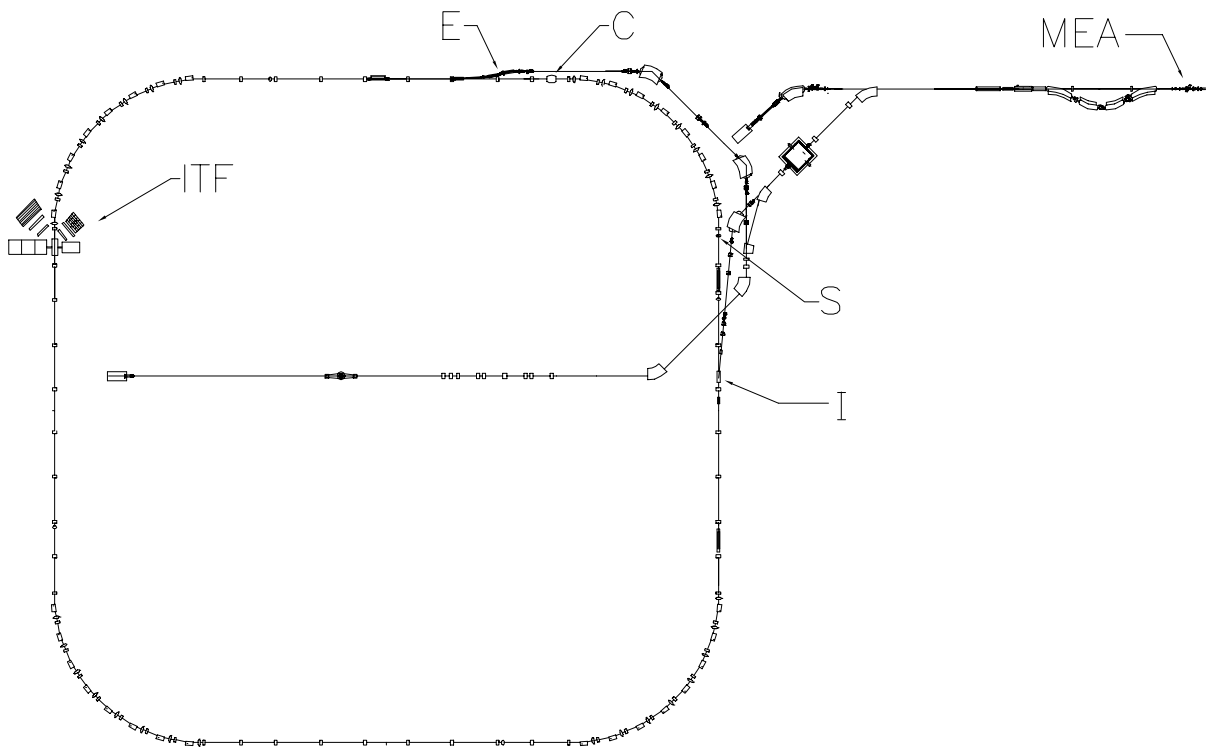### 3.1.2 Overview of the Amsterdam Pulse Stretcher (AmPS)

Figure 3.3: *A schematic layout of the AmPS electron storage ring at NIKHEF. The electrons from the accelerator MEA are injected in section I and can be extracted in section E. The apparatus for our experiment is located at the Internal Target Facility (ITF). Beam scrapers are installed in section S. Section C contains the 476 MHz cavity.*

The experiment was performed by using an unpolarized electron beam stored in AmPS (see Fig. 3.3) [87, 88]. This ring is an electron pulse stretcher with a circumference of 212 m. It is fed by a medium-energy electron accelerator (MEA) which can accelerate electrons up to energies of 770 MeV. Long beam lifetimes ($\sim$ 20 min) are obtained by compensating synchrotron radiation losses with RF power from a 476 MHz cavity in AmPS. In this way, a nearly 100% duty-factor electron beam with maximum energy of

900 MeV and current up to 200 mA (obtained by stacking and ramping) can be stored in the ring. Design parameters of AmPS are listed in Table 3.1.

Table 3.1: *Overview of design/operational parameters of MEA and AmPS.*

Parameter	Value	
E_{max} Linac	770	MeV
ring magnets	900	MeV
Beam loading	2.6	MeV/mA
Circumference	212	m
Revolution time	0.71	μs
Magnet radius	3.3	m
SR loss at 700 MeV	6.2	keV
RF frequency		
stretcher mode	2856	MHz
storage mode	476	MHz
SR damping at 700 MeV		
emittance	10^{-7}	m·rad
damping time	0.153	s
β_x at IP	2.2	m
β_y at IP	6.8	m
I_{Linac}	10	mA
Linac pulse length	2.1	μs
Injection rate	200	Hz
Beam duty factor	$\approx$100	%
$I_{Extracted}$ at 600 MeV	25	μA
I_{Stored}	200	mA
Lifetime	1200	s

The storage cell was located in the Internal Target Facility (ITF) where the ring lattice had minimum beta-function values of $\beta_x = 2.2$ m and $\beta_y = 6.6$ m. At the interaction region, the beam orbit can be shifted by using so-called local bumps which consist of two sets of steering magnets. In this manner the stored beam can be steered precisely through the center of a fixed storage cell.

A set of slits was installed at the opposite side of the ITF to reduce the beam halo. This resulted in an improvement of the background rates from beam scattering from the cell walls (See Section 3.3).

Currently, a polarized electron source is installed and polarized electron beam commissioning is in progress. In order to maintain the electron polarization in the storage ring, a 'Siberian snake' is installed in the ring. The polarimetry of the polarized electron

beam is realized by Compton laser back-scattering. Future experiments with polarized internal $^1\vec{\text{H}}, ^2\vec{\text{H}}$ and $^3\vec{\text{He}}$ targets and polarized electron beam are anticipated. Furthermore, in stretcher mode, continuous-wave (CW) electron beam can be extracted and used for experiments with external targets.

3.1.3 Principle of a storage cell target

The principal function of a storage cell is to increase the luminosity of an experiment without affecting the quality of the circulating beam. This is illustrated in Fig. 3.4. An intense polarized beam is injected into the feed tube of a T-shaped cell. The gas is confined by the cell to the region close to the stored beam axis, resulting in an increase of the areal target density by several orders of magnitude compared to the density of a free atomic beam.
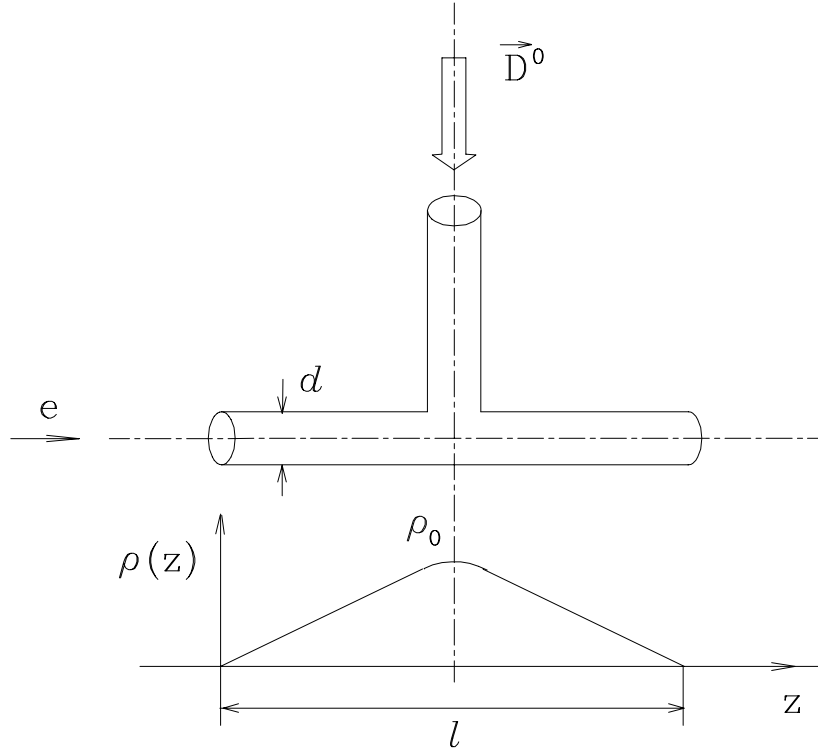

Figure 3.4: *Principle of a storage cell: gas is injected in the center of the T-shaped cell. The electron beam passes through the center of the windowless conductance limiter. The density distribution will be approximately triangular.*

Due to the gas dynamics, the target density $\rho(z)$ will have an approximately triangular distribution. The central density, ρ_0, can then be written as [89]

$$\rho_0 \simeq f_{\text{D}^0} \frac{1}{3C_0} \frac{l/2}{d^3} \sqrt{\frac{M}{T_{\text{cell}}}} = f_{\text{D}^0} \frac{1}{3C}, \tag{3.2}$$

where f_{D^0} (atoms/s) is the intensity of the injected deuterium beam with velocity v_{D^0}, l (cm) the length of the target cell, d (cm) the diameter, $M = 2$ (a.u.) the deuterium mass, T_{cell} (K) the cell temperature, $C_0 = 3.81 \times 10^3$ cm^3/s the conductance constant and the factor of 3 is due to the T-shape of the cell. Note that the density is independent of the velocity v_{D^0} of the injected beam. Consequently, the parameters that govern the luminosity can be written as

$$\mathcal{L} \simeq I_e f_{D^0} \frac{1}{3C_0} \frac{(l/2)^2}{d^3} \sqrt{\frac{M}{T_{cell}}}, \tag{3.3}$$

where I_e is the electron beam current. From this expression it is clear that one will try to minimize the diameter, increase the length, lower the temperature of the cell and maximize the circulating electron beam current in the storage ring. The minimum diameter of the storage cell is determined by the charge distribution of the stored electron beam, as will be discussed in Section 3.3, while the length of the cell is constrained by the detector acceptance as well as the variation of the beta-functions in the region near the interaction point. A detailed description of the construction of the storage cells used in our experiment is given in Sec. 4.2.1.

Compared to a free jet, the storage cell represents an improvement of more than two orders of magnitude in the luminosity. The luminosity of an experiment with a free jet can be characterized by

$$\mathcal{L} \simeq I_e f_{D^0} \frac{1}{2r_{D^0} v_{D^0}}, \tag{3.4}$$

where r_{D^0} is the radius of the free jet. For a storage-cell target the factor of improvement, γ, over a free jet can be written as

$$\gamma \simeq \frac{1}{3C_0} \frac{(l/2)^2}{d^3} \sqrt{\frac{M}{T_{cell}}} 2r_{D^0} v_{D^0}. \tag{3.5}$$

For our experiment, $l = 40$ cm, $d = 1.5$ cm, $T_{cell} = 100$ K, $M = 2$ a.u., $r_{D^0} \simeq 0.6$ cm and $v_{D^0} \simeq 10^5$ cm/s. Consequently, in our experiment we obtained $\gamma \simeq 350$.

For a cylindrical storage cell, the mean number of collisions of an atom with the walls is independent of atomic weight and cell temperature, and can be estimated from [90]

$$\langle N_c \rangle = \frac{3}{8}(\frac{l}{d})^2. \tag{3.6}$$

For a cell with a diameter of 1.5 cm and a length of 40 cm, the number of collisions amounts to about 270.

The dwell time of the polarized gas atoms in the storage cell is given by

$$t^{dwell} = N_c \tau^{stick} + t^{flight}, \tag{3.7}$$

where τ^{stick} is the mean sticking time per collision and t^{flight} the mean flight time of the atom (flying from the center to the exit of the cell). The latter can be expressed by

$$t^{\text{flight}} \simeq \frac{V_{\text{cell}}}{3C} = \frac{\pi}{16C_0} \frac{l^2}{d} \sqrt{\frac{T_{\text{cell}}}{M}}, \tag{3.8}$$

where V_{cell} is the volume of the T-shape cell. In our case, we have $t^{\text{flight}} \simeq 4$ ms. The mean sticking time depends on the characteristic binding energy E_{b} of an atom on the surface with temperature T_{cell} and is given by the Arrhenius' law [89, 91]:

$$\tau^{\text{stick}} = \tau_0 \exp^{E_{\text{b}}/k_B T_{\text{cell}}}, \tag{3.9}$$

where k_B is the Boltzmann constant and $\tau_0 \simeq 10^{-13}$ s. For a cell coated with Teflon ($E_{\text{b}} \simeq 30$ meV) at a temperature of 100 K, we have $N_c \tau_{\text{stick}} \simeq 10^{-9}$ s. This is negligible compared to t^{flight}. However, polarized atoms may depolarize during this period of time due to their interactions with local magnetic fields present at the surface of the cell material [92].

Since the dwell time is about 4 ms, only few events are lost when reversing the target polarization every 10 s. The polarization direction of the gas atoms was defined by an external magnetic field present over the entire cell length.

3.2 Monte Carlo Codes

Here, we present the Monte Carlo codes which were used to optimize the detector system, to study the detector resolutions and to interpret the experimental results.

The Monte Carlo codes contain five main parts: an event generator, calculation of cross section and counting rates, calculation and/or extrapolation of the asymmetries, resolution folding, and an interface with the PAW—CERN library [93]. There are slight differences among the codes used for elastic scattering, quasi-elastic scattering and Møller scattering from a deuterium target. Here, we only show some details of the codes used for the $^2\vec{\text{H}}(e, e'p)$ channel.

First we introduce the coordinate systems used in the codes. Fig. 3.5 schematically shows the setup with a storage cell, a proton detector ('p-det') and an electron detector (which is not shown in the figure for simplicity). A global (x_0, y_0, z_0) coordinate system is defined with the z_0-axis along the electron beam direction and the x_0-axis towards the electron detector and located in the plane defined by the cell and the center point of the electron detector. A 'mother' electron detector coordinate system (x'_e, y'_e, z'_e) can be obtained by a translation of the (x_0, y_0, z_0) system along the z_0-axis over a distance d_e followed by a rotation along the y_0-axis with an angle θ_e^0. Similarly, a 'mother' proton detector coordinate system (x'_p, y'_p, z'_p) can be defined by a translation of the (x_0, y_0, z_0) system along the z_0-axis over a distance d_p, followed by a rotation along the y_0-axis with

Figure 3.5: *Schematic representation of the coordinate systems used in the Monte Carlo codes. The electron detector is not shown for simplicity. See text for details.*

an angle θ_p^0, and a subsequent rotation along the z_0-axis with an angle of 180° (assuming coplanarity with the electron detector for simplicity).

The mother electron (proton) detector is defined virtually and has a height of $h_{e(p)}$, width of $w_{e(p)}$ and thickness of $t_{e(p)}$. The angular acceptance should be larger than any individual part (for example WC's and trigger scintillators) of the electron calorimeter (range telescope) as shown in Fig. 4.17. Those individual detector parts are treated in the codes using additional translations and Euler-rotations of the mother coordinate systems. These parts can be used as phase-space cuts on the event-rate simulation. In case of WC's, one can also use them to project event rates on each wire.

Events are simulated with electrons and protons in coincidence, and neutrons as recoil particles. An electron (proton) originates from a vertex located at a distance tz from the cell center and hits the front face of the mother electron (proton) detector at $(x'_{e(p)}, y'_{e(p)}, 0)$. Each event is kinematically treated in its own coordinate system (x, y, z), which is defined with the z-axis along the e-beam direction and the x-axis located in the scattering plane and pointing towards the electron side. Such a coordinate system is obtained by a translation of the (x_0, y_0, z_0) system along the z_0-axis over a distance tz, followed by a rotation along the z_0-axis with an angle ϕ_e. All the kinematic quantities are computed in this system which is labeled the 'laboratory' frame. When needed, the variables are boosted with the corresponding Lorentz parameters into the center of mass

system.

In order to predict the count rates and asymmetries, one has to evaluate the five-fold differential cross section (denoted as σ^5) shown in Eq. 2.60. The difficulty here is how to perform a five-fold integral over the extended target and detector phase space. It turns out that this can be treated uniquely in the Monte Carlo codes using the following procedures.

Firstly, a vertex z-position, tz, is randomly generated using a triangular density distribution over the storage cell region. If the electron beam has a size of σ_x and σ_y, then the vertex x- and y-positions are generated accordingly from the corresponding Gaussian distributions. Secondly, the hit positions of the mother electron (proton) detector are generated uniformly within the geometric acceptance $(-w_{e(p)}/2, +w_{e(p)}/2)$ and $(-h_{e(p)}/2, +h_{e(p)}/2)$. Then an electron (proton) track can be defined by the vertex position and the hit-point. Consequently, one can calculate $\theta_{e(p)}$ and $\phi_{e(p)}$. Thirdly, the scattered electron energy is uniformly generated within an energy acceptance ΔE_e. The energy acceptance is estimated from data for the $^2\mathrm{H}(e, e'p)$ reaction obtained with our detector system.

In three-body kinematics, the highest allowed momentum of one of the outgoing particles is limited by

$$(p_1^{\mathrm{cm}})_{\mathrm{max}} = \frac{1}{2E_{\mathrm{cm}}} \sqrt{(E_{\mathrm{cm}}^2 - (m_2 + m_3 - m_1)^2)(E_{\mathrm{cm}}^2 - (m_2 + m_3 + m_1)^2)}, \tag{3.10}$$

where E_{cm} is the total energy in the three-body center of mass system and m_i are the masses of the three particles. For electrons of the $^2\mathrm{H}(e, e'p)$ reaction, Eq. 3.10 obviously reduces to

$$(p_e^{\mathrm{lab}})_{\mathrm{max}} \approx E_0, \tag{3.11}$$

where E_0 is the electron beam energy.

Given five kinematic quantities for three outgoing particles (electron, proton and neutron), the remaining four can be calculated rigorously by using conservation of four-momentum. Namely, one has

$$\begin{aligned}
\sum_i p_i \sin \theta_i \cos \phi_i &= 0 \\
\sum_i p_i \sin \theta_i \sin \phi_i &= 0 \\
\sum_i \sqrt{p_i^2 + m_i^2} &= E_0 + M_d \\
\sum_i p_i \cos \theta_i &= \sqrt{E_0^2 - m_e^2},
\end{aligned} \tag{3.12}$$

where $i = e, p, n$. With p_e, θ_e, ϕ_e, θ_p and ϕ_p known, one can then calculate p_p, and consequently p_n, θ_n and ϕ_n. In principle, Eq. 3.12 is a quadratic relation and there will be possibilities of having two solutions, which correspond to proton and neutron

knock-out as treated in the PWBA. Both solutions are accounted for in our simulation codes.

The event rates are calculated as follows. One starts from the relations

$$
\begin{aligned}
\int_{-w_p/2}^{+w_p/2} \int_{-h_p/2}^{+h_p/2} \frac{d\sigma}{dx'_p dy'_p} &= \frac{1}{d_p^2} \int_{(\theta'_p)_{\min}}^{(\theta'_p)_{\max}} \frac{d\sigma}{d\theta'_p d\phi'_p} \\
&= \frac{1}{d_p^2} \int_{\theta_p^{\min}}^{\theta_p^{\max}} \frac{d\sigma}{\sin\theta_p d\theta_p d\phi_p} \frac{d_p'^{\,3} - d_p'^{\,2}\cos\theta'_p tz}{(d_p'^{\,2} + tz^2 - 2d_p'tz\cos\theta'_p)^{3/2}} \frac{\tan\phi_p}{\tan\phi'_p} \\
&= \frac{1}{d_p^2} \int_{\theta_p^{\min}}^{\theta_p^{\max}} \frac{d\sigma}{\sin\theta_p d\theta_p d\phi_p} J_p,
\end{aligned} \tag{3.13}
$$

where θ'_p and ϕ'_p are defined in Fig. 3.5, and $d'_p = \sqrt{d_p^2 + x'^{\,2}_p}$. If tz, w_p and h_p are all small ($\ll d_p$), then the Jacobian $J_p \approx \sin\theta_p$ as expected. Note that $\int \frac{d\sigma}{\sin\theta_p d\theta_p d\phi_p}$ (and similarly $\int \frac{d\sigma}{\sin\theta_e d\theta_e d\phi_e}$) can now be directly related to the cross section σ^5. The right-hand side corresponds to the Monte Carlo integral. Therefore, the event rates n are given by

$$
n = \frac{w_p h_p w_e h_e \Delta E_e}{N} \sum_{i=1}^{N} \left(\frac{d\sigma}{dx'_e dy'_e dx'_p dy'_p dE_e} \right)_i = \frac{w_p h_p w_e h_e \Delta E_e}{N d_p^2 d_e^2} \sum_{i=1}^{N} (\sigma^5 J_p J_e)_i, \tag{3.14}
$$

where N is the total number of generated Monte Carlo events. Finally, the event rates can be binned as a function of any kinematic quantity, for example p_m, $\theta_{np}^{\mathrm{cm}}$, etc.

For the momentum density distribution of the nucleon inside the deuteron we use a parameterization of the data of Bernheim *et al.* (see Fig. 2.5 and 2.6). For missing momenta between 0 and 170 MeV/c, a cubic spline fit of the data was used. For missing momenta between 170 MeV/c and 340 MeV/c, a logarithmic straight-line fit was used, while for higher missing momenta a linear extrapolation of the fit was employed.

Using the Monte Carlo codes we studied the experiment for various detector and target configurations. From this we concluded that there was an advantage in using the range telescope as our proton detector system over the two hadron detectors existing at NIKHEF. Furthermore, the studies showed that there was no advantage in moving the proton detector around and we decided to place the range telescope at a fixed position. In addition, we concluded that the energy resolution of the electron calorimeter was not critical for reconstructing the missing momenta (see also chapter 6). In a later phase of the experiment, the Monte Carlo codes played an important role in interpreting the experimental analyzing powers.

3.3   Spatial Distribution of Stored Electron Beam

3.3.1   The slits system for measurements

Few data exist on the spatial distribution of stored electron beams. The intensity of the core of a damped electron beam is expected to follow a Gaussian distribution with σ-values in the order of 1 mm or less. Disturbing processes, such as rest-gas scattering and wake-field effects, will cause the intensity to drop off slower in the tails of the distribution. The contribution of such a halo determines the minimum diameter of a storage cell. Since the effective target thickness of the gas stored in a storage cell is inversely proportional to the cube of the cell diameter, it is essential to study the beam halo prior to installing such a cell.
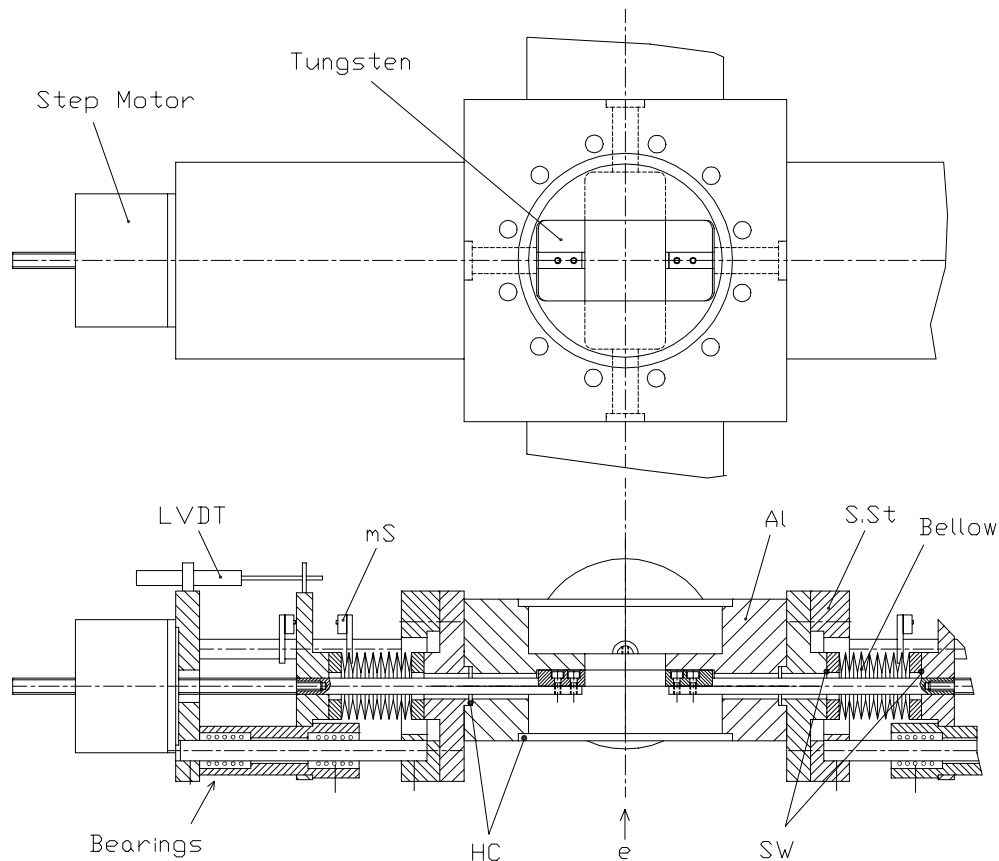
Figure 3.6:   *Schematical drawing of the slits system.   Top: view along the beam direction. Bottom: side view. mS: micro switch, HC: heliconflex seal, SW: stitch weld, Al: aluminum, S.St: stainless steel, LVDT: linear velocity and displacement transducer.*

Several test measurements have been performed with an electron beam stored in

AmPS. The goal of these tests was to obtain information on the spatial distribution of the stored beam, so that the diameter of the storage cell could be fixed. Therefore, a slits system was built, schematically shown in Fig. 3.6, and installed at the interaction point. It consists of 4 tungsten plates of 9.5 mm thickness. All four slits can be moved independently in or out using step motors. The slits are labeled 'up', 'down', 'in' and 'out' (with respect to the ring). The absolute positions of the slits are monitored by LVDTs. Micro-switches are installed to warrant the safety of the system. In a later stage of our experiment, the slits system was installed at another location of the ring as shown in Fig. 3.3.

3.3.2   Lifetime studies

To study the beam lifetime, we used the stored electron beam with an energy of 410 MeV, a lifetime of approximately 100 s and a peak current of about 10 mA. The electron beam current was measured using a Parametric Current Transformer (PCT)[1] [94].

Fig. 3.7 shows the beam lifetime as a function of the position of the slits. It can be seen clearly that in the domain where the slits were far away from the beam center, there was a negligible effect on the beam lifetime. When a slit intercepts a considerable fraction of the beam, the lifetime of the beam drops. When the slit is moved in further, the beam can no longer be stored.

The beam lifetime will decrease when an aperture size at the IT location is reduced [95]. The quantum lifetime of the beam, τ_q, can be related to the aperture size ($\pm x$) by

$$\tau_q = \frac{e^q}{2q}\tau_d,$$

(3.15)

with $q = (x/\sigma_x)^2/2$ and τ_d the damping time (for $E = 700$ MeV one has $\tau_d = 0.15$ s as listed in Table 3.1, while for $E = 410$ MeV one has $\tau_d \approx 0.40$ s). In general, the observed beam lifetime, τ_{exp}, can be written as

$$\frac{1}{\tau_{\mathrm{exp}}} = \frac{1}{\tau_q} + \frac{1}{\tau_0}.$$

(3.16)

Here, τ_0 is the so-called 'natural' beam lifetime e.g. due to scattering of the low-energy electrons from the residual gas. The dependence of the lifetime on x can be derived from Eq. 3.15 by solving the resulting expression for σ_x. Assuming a Gaussian distribution, one obtains after some arithmetic:

$$\sigma_x^2 = \frac{x}{\frac{\tau_0}{\tau_0 - \tau_{\mathrm{exp}}}\frac{\partial \ell n \tau_{\mathrm{exp}}}{\partial x} + \frac{2}{x}}.$$
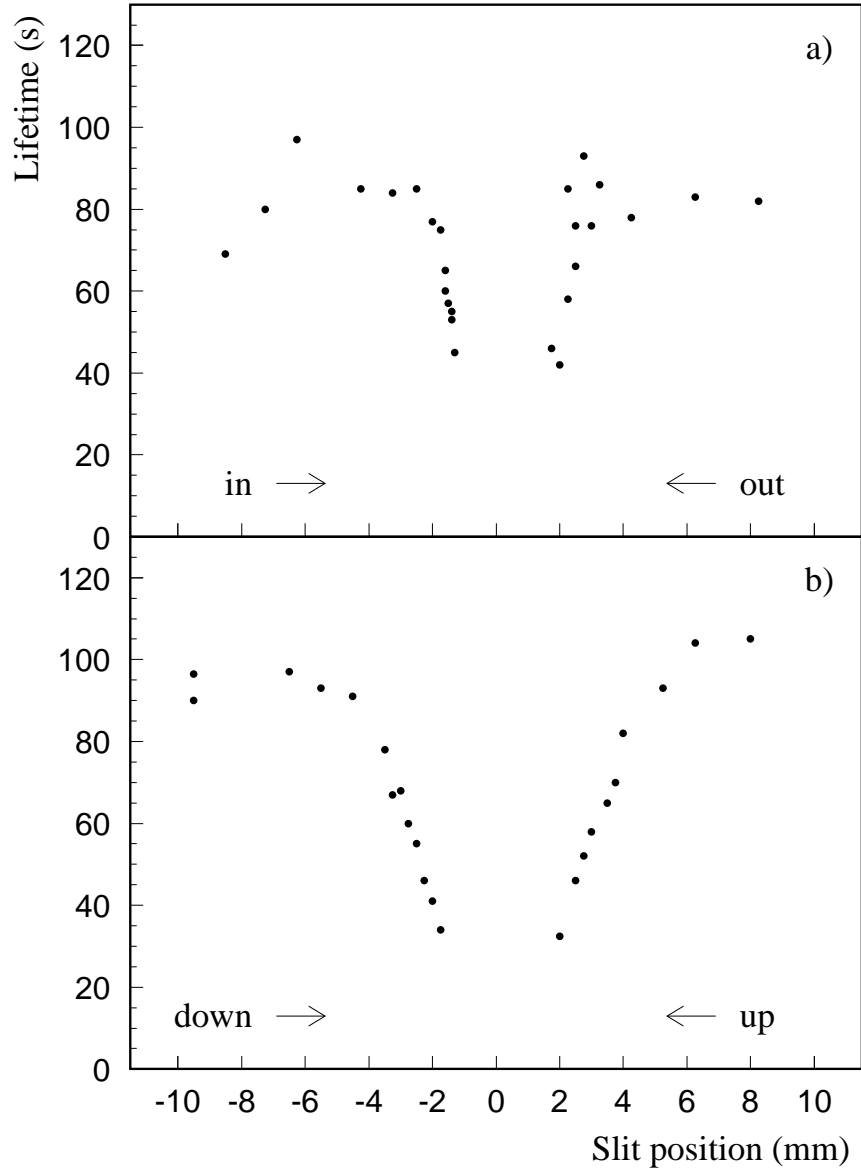
(3.17)

Figure 3.7: *Beam lifetime as function of the distance of the slits to the center of the beam.*

The $\sigma_{x(y)}$ deduced from the measured τ_{exp} values and the results for the 'in' ('down') slits are listed in Table 3.2 (3.3). The calculations have been limited to the region close to the beam center where the beam lifetime strongly depends on the position of the slits. We assumed $\tau_0 = 95$ s. The calculations yield $\sigma_x = 0.61 \pm 0.12$ mm and $\sigma_y = 1.13 \pm 0.20$ mm.

---

[1]Fabricated by Julien Bergoz, Crozet, 01170 Gex, France.

Table 3.2: σ_x *derived from the measured* τ_{exp}*-values for the 'in' slit.*

x (mm)	τ_{exp} (s)	$\dfrac{\triangle \ell n \tau_{\mathrm{exp}}}{\triangle x}$	$\overline{x}$ (mm)	$\overline{\tau}_{\mathrm{exp}}$ (s)	$\dfrac{\tau_0}{\tau_0 - \overline{\tau}_{\mathrm{exp}}}$	σ_x (mm)
1.30	45					
		> 1.82	1.35	49.5	2.088	0.51
1.40	54					
		> 0.54	1.45	55.5	2.405	0.74
1.50	57					
		> 0.92	1.55	59.8	2.695	0.64
1.60	62.5					
		> 1.21	1.68	68.8	3.619	0.55
1.75	75					

Table 3.3: σ_y *derived from the measured* τ_{exp}*-values for the 'down' slit.*

y (mm)	τ_{exp} (s)	$\dfrac{\triangle \ell n \tau_{\mathrm{exp}}}{\triangle x}$	$\overline{y}$ (mm)	$\overline{\tau}_{\mathrm{exp}}$ (s)	$\dfrac{\tau_0}{\tau_0 - \overline{\tau}_{\mathrm{exp}}}$	σ_y (mm)
1.75	34					
		> 0.752	1.875	37.5	1.652	0.90
2.00	41					
		> 0.460	2.125	43.5	1.845	1.09
2.25	46					
		> 0.712	2.375	50.5	2.135	1.00
2.50	55					
		> 0.348	2.625	57.5	2.533	1.26
2.75	60					
		> 0.360	2.925	64.0	3.065	1.28
3.05	68					
		> 0.343	3.300	73.0	4.318	1.26
3.50	78					

Similar results can be obtained from the measurements with the 'out' and 'up' slits as shown in Fig. 3.7. The error of about 20% in the results is partly due to the accuracy of the lifetime measurements. The obtained $\sigma_{x(y)}$-values in Table 3.2 (3.3) do not deviate much from each other over the measured x(y)-range, and one can conclude that the

charge distribution of the beam in the region close to the beam center $(x, y < \pm 3\sigma_{x,y})$ is a Gaussian function. This region contains more than 99% of the stored electrons.

The equilibrium electron beam size can be used to determine the beam emittance, since

$$\sigma_{x(y)} = \sqrt{\beta_{x(y)} \epsilon_{x(y)}}, \tag{3.18}$$

where $\beta_{x(y)}$ is the beta function and $\epsilon_{x(y)}$ the emittance of the electron beam in the horizontal (vertical) direction. The values of the beta functions from Table 3.1 yield $\epsilon_x = 1.69 \pm 0.66 \times 10^{-7}$ m·rad and $\epsilon_y = 1.87 \pm 0.66 \times 10^{-7}$ m·rad.

The emittance of the electron beam at injection is given by

$$\epsilon_{\mathrm{MEA}} = 2 \times 10^{-5} \frac{1}{E} \quad \mathrm{m \cdot rad}. \tag{3.19}$$

For a 410 MeV beam, one calculates 0.48×10^{-7} m·rad, which is about a factor of 3.5 smaller than the 'measured' values.

The emittance of a damped beam is determined by the specific magnetic lattice [88]. One has

$$\epsilon_x = C_q \gamma^2 \frac{I_5}{I_2 - I_4}, \tag{3.20}$$

where the Lorentz quantity γ denotes the beam energy, $C_q = \frac{55}{32\sqrt{3}} \frac{\hbar}{m_e c^2} = 3.86 \times 10^{-13}$ m and I_i are synchrotron integrals, which are lattice-dependent parameters. For AmPS, $\frac{I_5}{I_2 - I_4} = 0.13$. In an uncoupled situation (corresponding to a 'flat beam spot') we will have $\epsilon_y \ll \epsilon_x$, whereas for complete coupling ('round beam spot') the emittance will be shared so that $\epsilon_y^s = \epsilon_x^s = \epsilon_x/2$. Numerically, for a 700 MeV beam, ϵ_x amounts to 1.0×10^{-7} m·rad, while for a 410 MeV beam, one has 0.32×10^{-7} m·rad. This is significantly smaller than the 'measured' values.

Consequently, the large emittance cannot be due to strong coupling only. A possible explanation may be given by the presence of the residual gas in the ring. Especially, during the beam lifetime measurements, the ring vacuum was not optimal. The ring became operational shortly after a shut-down period and most of the ion-collectors were not operational. A vapor pressure of 5×10^{-8} mbar partial H_2O in the ring represents an effective target thickness of about 3×10^{13} H_2O molecules·cm^{-2}. According to Lác [96], the emittance growth can amount to 7×10^{-14} m·rad per revolution for 10^{14} H_2O molecules·cm^{-2}. Therefore, the emittance will already reach the 'measured' values within about 5 seconds.

A poor ring vacuum might also explain the observed beam lifetime of approximately 100 s. In the preceding running period, most of ion-collectors became operational and more vacuum pump stations were installed along the entire ring, especially in the

curved sections. The vacuum pressure improved drastically. With the installation of the 476 MHz cavity, the synchrotron radiation loss was compensated so that a beam lifetime of more than 1000 s was reached. More emittance measurements have been made by the AmPS accelerator group. Note that the ring was initially designed to run experiments in extraction mode. However, with the present emphasis on internal target physics, a plan was developed to change the excitation of magnets in order to improve the damped emittance.

3.3.3   Study of cell-wall background

Next, the beam halo distribution was studied. Two scintillator telescopes, each consisting of two 2 mm thick plastic scintillators, located in the horizontal (vertical) plane at an angle of 20° (38°) and covering a solid angle of 45 (20) msr, were placed at the IP.

The coincident count rate was measured in each telescope as a function of slit position. In Fig. 3.8 the count rates are shown for the four slits. All measurements show a similar behavior when a slit is moved in: a constant background rate until a position is reached at which the count rate starts to increase drastically. Finally, the photomultipliers had to be switched off due to the high rate.

The count rates in the horizontal telescope were about a factor of 10 higher than the rates in the vertical one. This holds for both the 'up/down' and 'in/out' slits, and can be explained by scattering angle and phase-space differences of the telescopes.

The count-rate data show that the beam distribution has long tails (the so-called 'beam halo'), extending over 20 (10) times the σ_x (σ_y) values obtained from Table 3.2 (3.3). This indicates that the tails cannot be described by Gaussian distributions, especially for the x- (horizontal) plane. The fact that the horizontal plane ($20 \times \sigma_x$) is worse than the vertical plane ($10 \times \sigma_y$) probably confirms that synchrotron radiation losses form a major contribution to the beam halo. Note that σ_y is about a factor of two larger than σ_x (since $\beta_y > \beta_x$). The count rates for both x- and y-planes start to increase almost at the same distance away from the beam center. Therefore, we concluded that an elliptically shaped storage cell was not necessary and a cylindrical cell was used.

From the count-rate measurements and Monte Carlo simulations using the CERN GEANT-package [97], we estimated that with a storage cell of 15 mm diameter and 25 μm wall thickness the $(e, e'p)$ background rate from the cell walls would be about 10-30% of the rate from the polarized deuterium target. Conservatively, we started the first measurements with a storage cell of 25 mm diameter and 100 μm thickness. Shortly after, we used storage cells of 20 mm diameter and 25 μm thickness. Finally, with emphasis on the physics of elastic e-$\overleftrightarrow{d}$ scattering, we used storage cells of 15 mm diameter.

In order to further reduce the background rates (from beam scattering from the cell walls), it proved important to use the slits to scrape the beam halo. This will be discussed next.
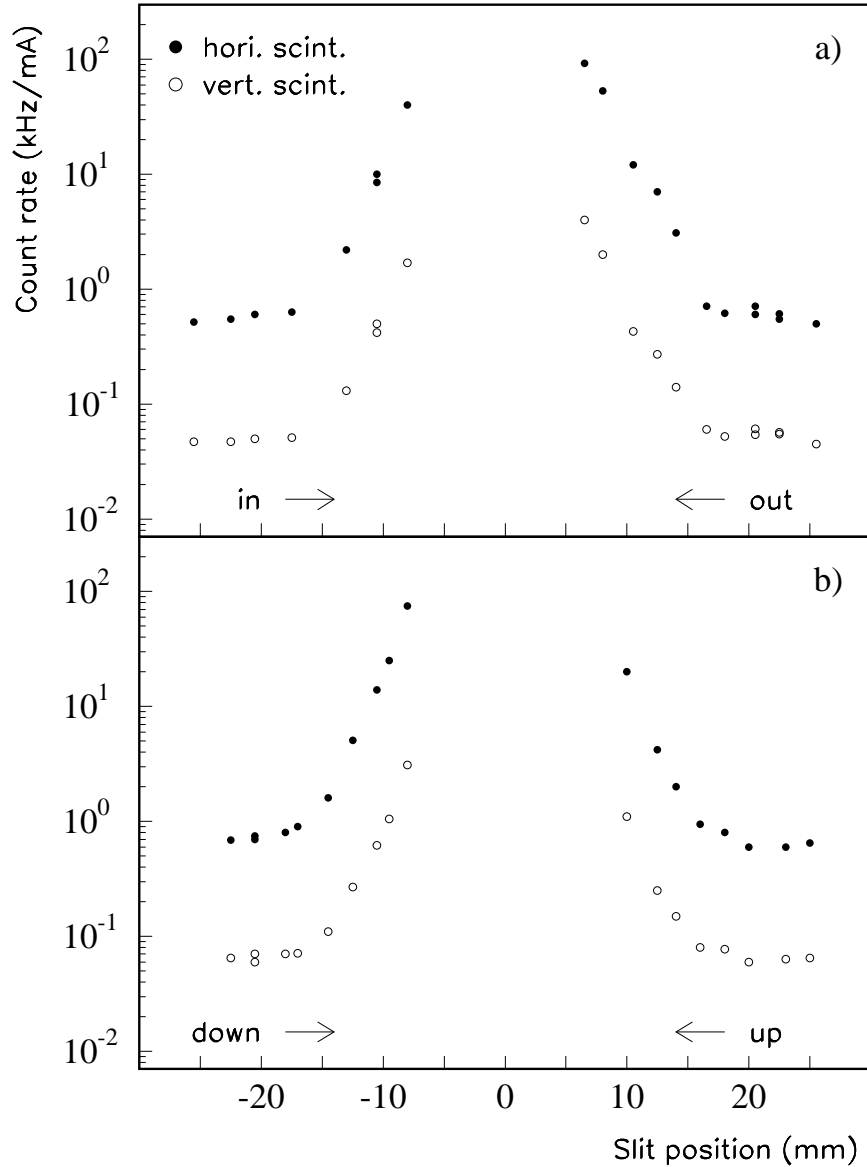
Figure 3.8: *Count rates (kHz/mA) in the horizontal and vertical scintillator telescopes as function of the distance of the horizontal and vertical slits to the center of the beam.*

3.3.4 Effects of beam scraping

The slits system was moved from the IT location to the opposite side in AmPS as shown in Fig. 3.3. A storage cell target and the detector system (as shown in Fig. 4.17) were installed at the IP. The measurement employed a storage cell of cylindrical shape with a wall thickness of 100 μm, a diameter of 20 mm and a length of 400 mm.

The investigation was performed by studying the $(e, e'p)$ rates while changing the
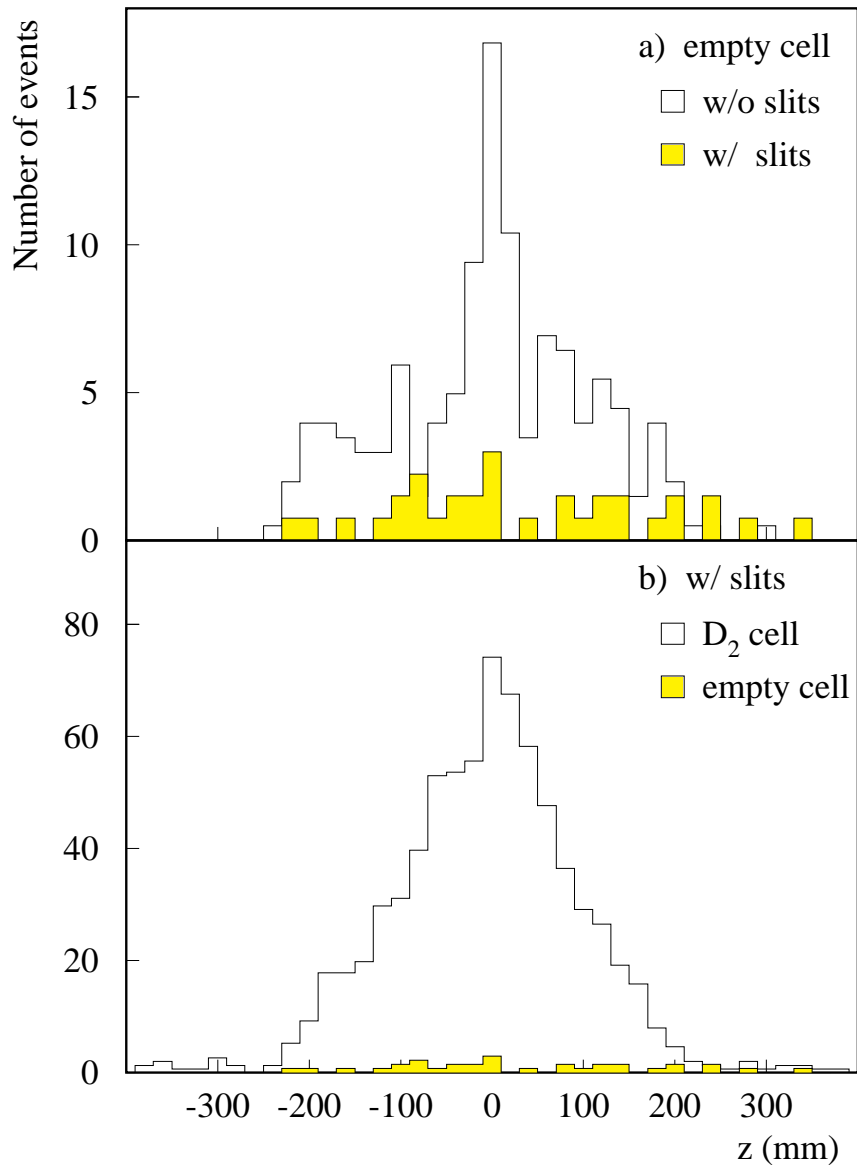
Figure 3.9: *Event distribution as a function of the vertex z-position for $(e, e'p)$ scattering from a storage cell with a diameter of 20 mm. a) empty cell measurements with (hatched histogram) and without (blank histogram) the slits; b) comparison of a D_2 gas target and the empty cell with the slits in place for scraping the beam halo.*

settings of the slits. The first measurement was for an empty storage cell, with the slits completely out. The full beam halo was allowed to hit the storage cell. The second measurement was also for an empty cell, but with the slits moved in to scrape away part of the beam halo. All four slits were moved in to about 6 mm from the beam center

(hereafter referred to as the 'closed' position). These positions were chosen such that the singles rates in both the CAL- and RT- arms were minimal, while not hampering the injection of the electron beam. The third measurement was for a D_2 gas target with the slits in 'closed' position. D_2 was provided through a capillary from a buffer volume directly into the center of the storage cell (see chapter 4). The gas flux was about eight times higher than that of the ABS.

In order to understand the following, we give a brief outline of the data analysis (for a full discussion see chapter 6). Only coincident events with tracks in both proton and electron arms are selected. We require that there is substantial energy deposited in the electron calorimeter. Protons are selected using correlations of the ADC values from the RT scintillator array. Then cuts are applied on the coincident timing (TOF of protons/deuterons/electrons) and the transverse vertex distance.

Fig. 3.9 shows the $(e, e'p)$ event distribution as a function of the vertex z-position. The distributions are normalized using the integrated beam currents from the PCT. In Fig. 3.9.a) we compare the two measurements with the empty cell. The hatched histogram corresponds to the data obtained with 'closed' slits, while the open histogram is for the measurement with 'open' slits. Due to the presence of the feed-tube, we observe more events around $z = 0$ mm. Clearly, closing the slits results in a factor of 4.5 reduction in the total number of events. In Fig. 3.9.b) the measurement of the empty cell with 'closed' slits (hatched histogram) is compared with the measurement for a D_2 target (open histogram). The $(e, e'p)$ event distribution for D_2 shows the expected triangular shape (see also Fig. 3.4), while the empty cell distribution is as one expects for cell-wall events. Comparing the total number of events for the two measurements, we conclude that the background contribution in the D_2 measurement is 3-4%. Therefore, we expect that the background contribution for an ABS measurement will be about 25-30% using a storage cell with a wall thickness of 100 μm. The background will reduce to less than 10% when a 25 μm cell is used.

3.3.5 Møller electrons

The cross section for Møller scattering, namely electron-electron scattering, can be precisely calculated from QED. In an electron scattering experiment where non-magnetic spectrometers are used Møller scattering is the prime source of background. Therefore, it is important to demonstrate that it is possible to operate our detector setup in such an environment.

The kinematics for Møller scattering is determined once the scattering angle is known. The energy of the scattering electrons in the laboratory system can be written as

$$E_{\text{lab}} = \gamma^2 m_e + \gamma^2 \beta^2 m_e \cos \theta_{\text{cm}}. \tag{3.21}$$

Here β and γ are the Lorentz quantities for the center-of-mass system moving with respect
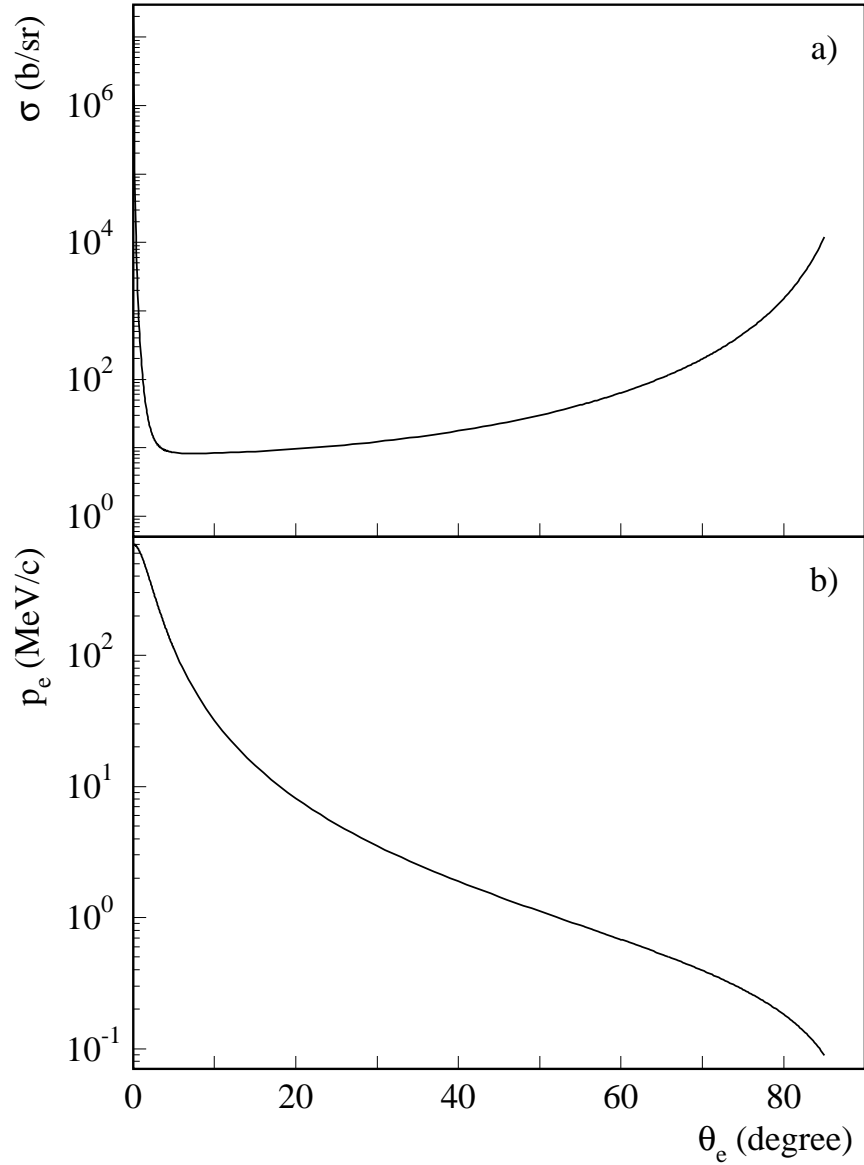
Figure 3.10: *The cross section (a) and momentum (b) of scattered Møller electrons as a function of laboratory angle for 700 MeV electrons incident on deuterium atoms.*

to the laboratory system. The relation between θ_{lab} and θ_{cm} is given by

$$\tan \theta_{\mathrm{lab}} = \frac{\sin \theta_{\mathrm{cm}}}{\gamma(1 + \cos \theta_{\mathrm{cm}})}. \tag{3.22}$$

The cross section in the laboratory system can be obtained from

$$\frac{d\sigma}{d\Omega_{\text{lab}}} = \frac{d\Omega_{\text{cm}}}{d\Omega_{\text{lab}}}\frac{d\sigma}{d\Omega_{\text{cm}}} = \frac{d\Omega_{\text{cm}}}{d\Omega_{\text{lab}}}\frac{\alpha^2}{4E_{\text{cm}}^2}\left[\frac{1}{\sin^4\frac{\theta_{\text{cm}}}{2}} + \frac{1}{\cos^4\frac{\theta_{\text{cm}}}{2}} + 1\right]. \qquad (3.23)$$

The factor $\dfrac{d\Omega_{\text{cm}}}{d\Omega_{\text{lab}}}$ defines the transformation of solid angles between the laboratory and center-of-mass systems, and α is the fine-structure constant. Since E_{cm} can be calculated from the incident electron energy by using a Lorentz transformation and θ_{cm} is given by Eq. 3.22, both E_{lab} and $\dfrac{d\sigma}{d\Omega_{\text{lab}}}$ can be evaluated directly in the laboratory system as a function of the scattering angle θ_{lab}.

In Fig. 3.20, the cross section and momentum distribution of Møller electrons are plotted as a function of scattering angle for 700 MeV incident energy. At a laboratory angle of about 5° one can distinguish between backward and forward scattering. Since the angular region covered in our experiment is from 20° to 70° (see Fig. 4.17), backward Møller scattering dominates. The backward scattered Møller electrons have fairly low momenta. Therefore, we placed a thin metal foil in front of the vertex MWPC which blocked most of the Møller electrons without affecting the high-energy electrons corresponding to the $(e, e'p)$ and $(e, e'd)$ channels. For the proton/deuteron side, since the protons and deuterons give relatively large signals on the wires, the effect of low-energy Møller electrons will be small for appropriately chosen threshold settings of the wire-chamber discriminators.

Electron rates were simulated using a Monte Carlo code in which the vertex generator included Møller scattering. The calculation predicts that a cut-off momentum of 1 MeV/c yields a counting rate of ∼10 kHz/wire in the most forward area of the vertex MWPC of the electron arm. Such rates can be handled by our detector system.

3.4   Target Design Considerations

We have shown in Sec. 3.1.3 the principle of a storage cell target and in Sec. 3.3 we showed studies of the electron beam spatial distribution. One of major tasks in our experiment was to build a tensor polarized deuterium target. We made a choice of using an existing atomic beam source (ABS) containing two sextupole magnets to feed our storage cell target with an intensive flux of polarized deuterium atoms. We considered optimizations of the sextupole focusing optics to increase the atomic flux (intensity), constructed a polarization scheme with the highest figure of merit ($\Delta P^2 I$, I = atomic beam intensity, ΔP = polarization difference between the two polarization states of the experiment), and measured the absolute target polarization with several techniques. In

the following, we will discuss some considerations, which are essential in the design of a polarized deuterium internal target.

The structure of deuterium atomic hyperfine states is well known. The interaction hamiltonian of the coupled nuclear and electron spins ($\vec{I}$ and $\vec{J}$) arising in a static magnetic field $\vec{B}$ is

$$H_{stat} = \frac{2\,h\,\nu_0}{3}\,\vec{I}\cdot\vec{J} + \mu_B(g_I\,\vec{I} + g_J\,\vec{J})\cdot\vec{B}. \tag{3.24}$$

Here, $g_I = -0.00047$ and $g_J = 2.0023$ are the gyromagnetic factors, μ_B is the Bohr magneton and

$$h\,\nu_0 = \mu_B(g_J - g_I)B_c, \tag{3.25}$$

where the critical field B_c characterizes the strength with which the two spins interact ($B_c = 11.7$ mT).

The energy eigenstates for deuterium can be expressed as linear combinations of the eigenvectors of the spin operators $\vec{I}$ and $\vec{J}$:

$$\begin{aligned}
|\,1\rangle &= |\,1,\tfrac{1}{2}\rangle\,, \\
|\,2\rangle &= \alpha_{-+}\,|\,1,-\tfrac{1}{2}\rangle + \alpha_{++}\,|\,0,\tfrac{1}{2}\rangle\,, \\
|\,3\rangle &= \alpha_{--}\,|\,0,-\tfrac{1}{2}\rangle + \alpha_{+-}\,|-1,\tfrac{1}{2}\rangle\,, \\
|\,4\rangle &= |-1,-\tfrac{1}{2}\rangle\,, \\
|\,5\rangle &= \alpha_{+-}\,|\,0,-\tfrac{1}{2}\rangle - \alpha_{--}\,|-1,\tfrac{1}{2}\rangle\,, \\
|\,6\rangle &= \alpha_{++}\,|\,1,-\tfrac{1}{2}\rangle - \alpha_{-+}\,|\,0,\tfrac{1}{2}\rangle\,,
\end{aligned} \tag{3.26}$$

where

$$\begin{aligned}
\alpha_{+\pm} &= \sqrt{\tfrac{1}{2}(1 + a_\pm)} & \alpha_{-\pm} &= \sqrt{\tfrac{1}{2}(1 - a_\pm)}\,, \\
a_\pm &= (x \pm \tfrac{1}{3})/\sqrt{1 \pm \tfrac{2}{3}x + x^2} & x &= \frac{B}{B_c}\,.
\end{aligned} \tag{3.27}$$

The energy of these states for a deuterium atom in a magnetic field are shown in Fig. 3.11. At zero magnetic field, the two possible total spin states $F = 1 \pm \frac{1}{2}$ ($\vec{F} = \vec{I} + \vec{J}$) are $(2F+1)$-fold degenerate. The energy splitting between the two levels is $\nu_0 = 327.4$ MHz. In a non-zero magnetic field this degeneracy is lifted. In the weak field limit ($B \ll B_c$), the interaction with the external field can be treated as a perturbation with respect to the coupling between the two spins. Each of the two multiplets splits into $2F + 1$
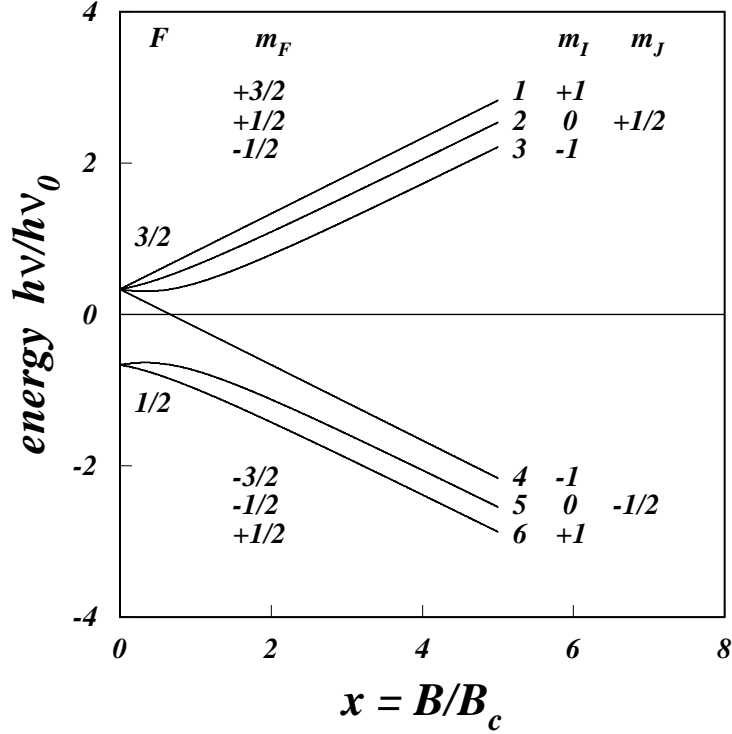
Figure 3.11: *Hyperfine structure of deuterium as function of the reduced static field $x = B/B_c$ ($\nu_0 = 327.4$ MHz). The spin quantum numbers F, m_F (m_I, m_J) are indicated for the weak (strong) field limit on the left (right) side of the figure.*

energy substates separated by equal energies of 9.3 MHz/mT and characterized by the projection quantum number m_F of the total spin along the magnetic field. At large B ($B \gg B_c$), the electronic and nuclear spins decouple as the interaction with the external field becomes dominant. It is only in this limit that the spin projections m_J and m_I will be 'good' quantum numbers.

At the target location a magnetic field is provided to define the nuclear spin direction. The nuclear polarization of an ensemble of atoms is then entirely determined by the strength of such a holding field and by the relative populations n_k ($k = 1, ...6$) of the hyperfine states. Fig. 3.12 shows P_z and P_{zz} for the various hyperfine states as function of the magnetic field strength. The ensemble average (denoted here by double brackets) of the vector polarization is given by

$$P_z = \langle\langle I_z \rangle\rangle = n_1 + \alpha_{-+}^2 n_2 - \alpha_{+-}^2 n_3 - n_4 - \alpha_{--}^2 n_5 + \alpha_{++}^2 n_6 = n_+ - n_-$$

$$(3.28)$$

and of the tensor polarization by

$$P_{zz} = \langle\langle 3I_z^2 - 2 \rangle\rangle = 1 - 3(\alpha_{++}^2 n_2 + \alpha_{--}^2 n_3 + \alpha_{+-}^2 n_5 + \alpha_{-+}^2 n_6) = 1 - 3n_0,$$
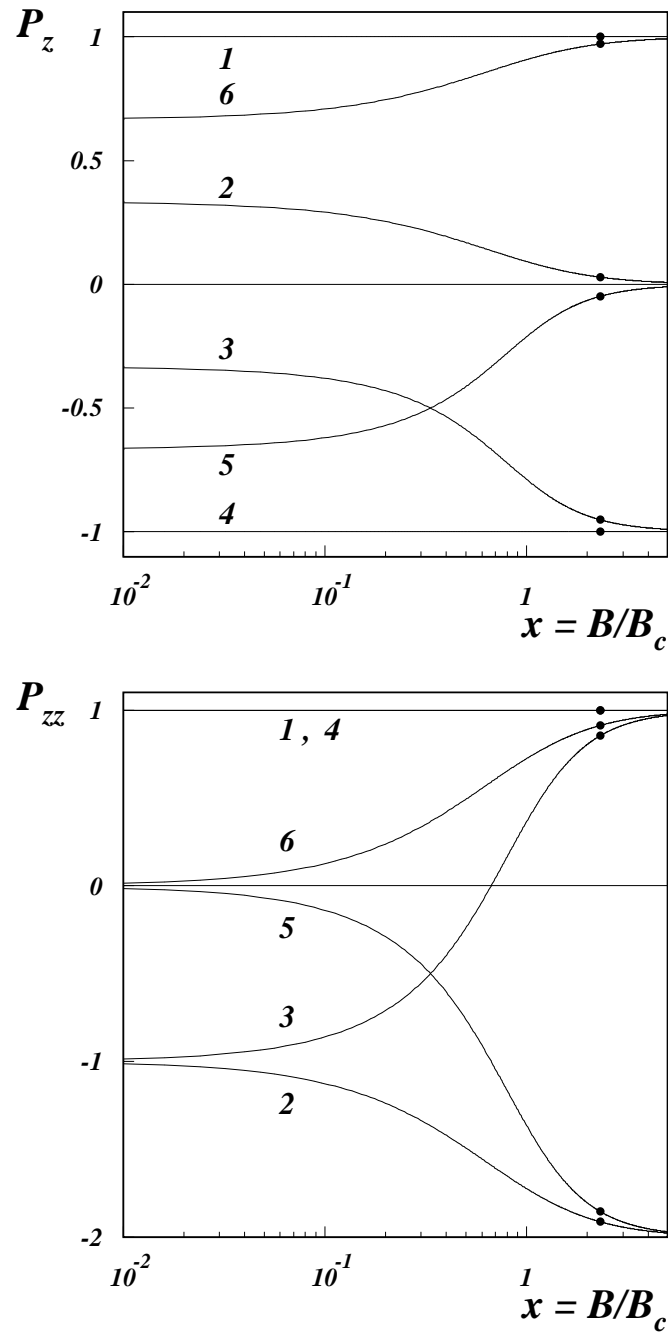
$$(3.29)$$

Figure 3.12: *Vector and tensor polarization of the deuterium hyperfine states as function of the reduced static field. The dots show the polarization values for 27 mT, the working point of our tensor polarized $^2H(e, e'p)$ internal target experiment.*

where $n_{\pm,0}$ are the probabilities of finding the nuclear spin in the various nuclear spin substates $m_I = \pm 1, 0$. We chose $B = 27$ mT ($\approx 2.3 B_c$) for our 'strong' target holding field. Obviously, with all six hyperfine states equally populated, one obtains zero tensor and vector polarization. Therefore, one needs to manipulate the hyperfine states of the target atomic ensemble before feeding atoms into the storage cell. This can be achieved by using sextupole magnets and RF transition units.

3.4.1 Focusing and rejection of atoms by using sextupole magnets

To get more insight into the properties of the Stern-Gerlach magnets, a raytracing code was written which computes the trajectories of the atoms (H or D) throughout the various elements of the ABS and the target cell.

The relative beam flux at the exit of the nozzle for atoms with velocities between v and $v + dv$ is assumed to be of the form [98]

$$f(v) = 2\frac{v^3}{\xi^4}\, e^{-\dfrac{(v - v_0)^2}{\xi^2}}, \tag{3.30}$$

where $\xi = \sqrt{2 k_B T \alpha / m}$, T is the temperature of the nozzle (≈ 70 K), and v_0 and α are parameters for super-sonic jet flow. The program uses the velocity distribution measured at ETH [99] and MPI [100] to generate the starting conditions of the atoms at the nozzle.

For a sextupole magnet the radial dependence of the magnetic field is assumed to be of the form

$$B(r) = B_0(z)\left(\frac{r}{r_0}\right)^2, \tag{3.31}$$

where r is the distance to the beam axis denoted by z, $B_0(z)$ the pole-tip field and r_0 the pole-tip radius. The algorithm is based on a fourth-order Runge-Kutta iteration of the equation of motion

$$m\frac{d^2 r}{dt^2} = 2\,\mu_{\text{eff}}\, B_0\, \frac{r}{r_0^2}. \tag{3.32}$$

Here

$$\mu_{\text{eff}} = \pm \frac{\dfrac{2m_F}{2I + 1} + x}{\sqrt{1 + \dfrac{4m_F}{2I + 1}x + x^2}}\, \frac{g}{2}\, \mu_B \tag{3.33}$$

is the effective magnetic moment of the atom [101]. For hyperfine states 1, 2, and 3 (4, 5 and 6), one has that $\mu_{\text{eff}} > 0$ (< 0), and consequently atoms in those states will be focused (defocused) when they pass through a sextupole magnet.
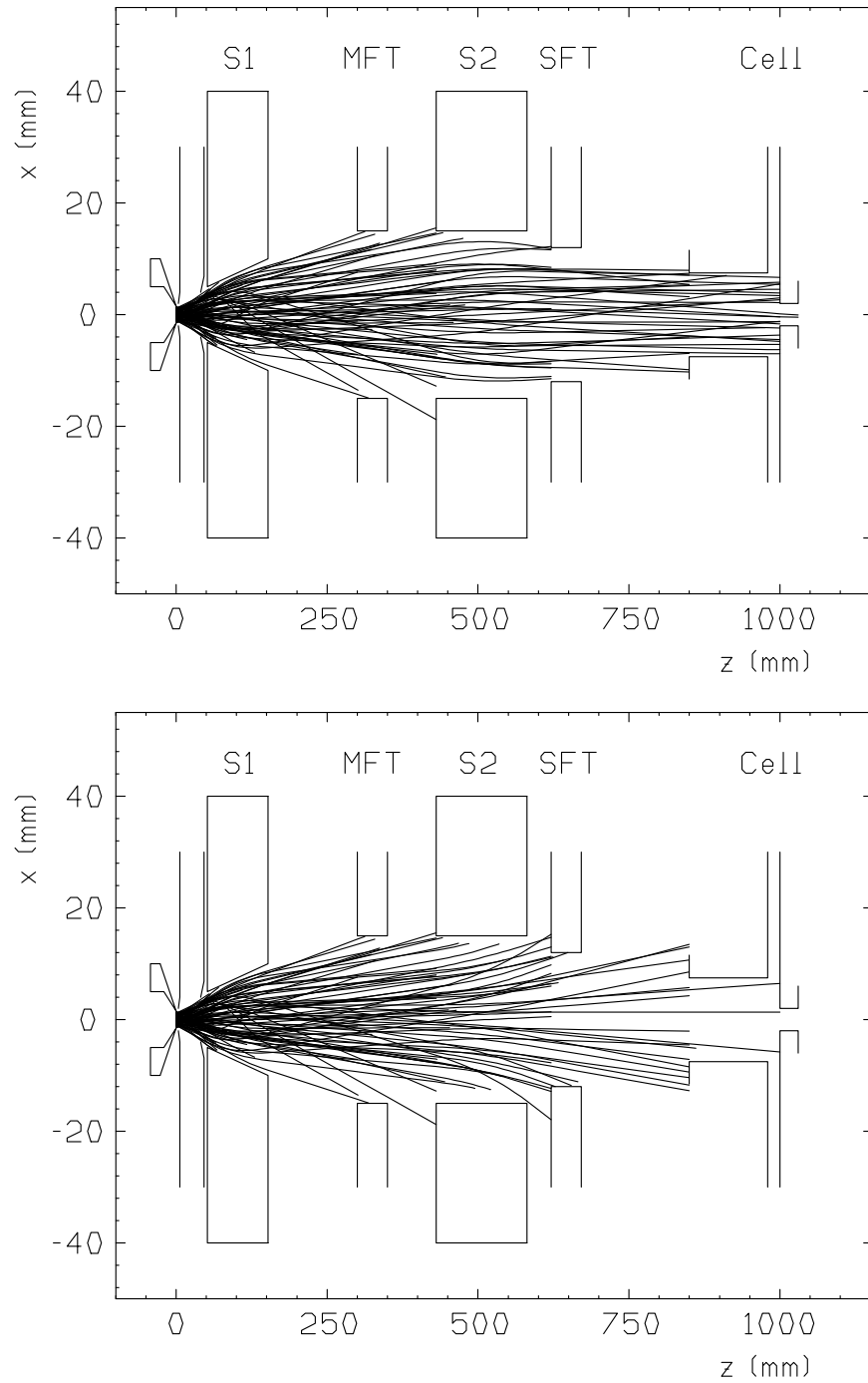
Figure 3.13: *Trajectories of deuterium atoms (in hyperfine state 1 only) throughout the ABS elements calculated with the raytracing codes described in the text. Note that the transverse dimensions (x-axis) are magnified. S1, S2: sextupole magnets; MFT, SFT: RF-transition units. MFT 1-4 transition is switched off (top) and on (bottom).*

The output of such a calculation for our setup is illustrated in Fig. 3.13. At the top it shows trajectories of atoms populated in hyperfine state 1 with the MFT 1-4 transition is switched off. One sees that the atoms are focused by the two sextupole magnets into the feed-tube of the storage cell. At the bottom the same trajectory calculation is repeated with the MFT 1-4 transition switched on. After the transition, most of atoms are defocused by the second sextupole magnet and remain outside the acceptance of the feed-tube.

This program permits to optimize the design of focusing magnets for a given nozzle temperature and feed-tube geometry.

3.4.2   Polarization scheme

Among the different RF transition schemes which can deliver polarized deuterium beams with tensor or vector polarization switchable between maximal values, the schemes shown in Table 3.4 offer the highest figure of merit with the least number of RF transition units. In particular, for tensor polarized deuterium only one MFT and one SFT are needed, in which case the MFT is used for a 1-4 transition (positive gradient) inbetween the sextupoles in order to eliminate hyperfine state 1, while the SFT is then used to flip P_{zz} from -2 to $+1$ with the σ-transitions 3-5 and 2-6. The magnetic holding field at the target has to be strong compared to the critical field of deuterium.

While the figure of merit dramatically decreases for tensor polarized targets when the target holding field is decreased, for vector polarized deuterium only a factor close to 1.5 is lost by choosing a weak target holding field. Therefore, both a strong or a weak holding field can be used at the target when working with vector polarized deuterium. The polarization can be produced as follows: firstly, state 3 is eliminated with a 3-4 MFT[2] before the second sextupole. Next, for a weak target holding field, the 2-6 SFT is continuously on, while the WFT (positive gradient) is switched on and off to reverse P_z from $+5/6$ to $-5/6$. For a strong holding field we alternatively use the 2-6 SFT and the WFT, obtaining $P_z = +1$ or -1. This last scheme requires operating a WFT in an environment with strong magnetic fringe fields. Note that the ABS equipped with the MFT and the WFT also allows to produce a maximally vector polarized hydrogen beam.

---

[2]This transition can be achieved either with a positive gradient and an RF cutoff upstream of the RF coil to inhibit the transitions 1-2 and 2-3, or, more simply, with a negative gradient (the first two encountered transitions 1-2 and 2-3 do not affect the populations of states 1, 2 and 3).

Table 3.4: *RF transition schemes for producing tensor and vector polarized deuterium beams. For each scheme, the columns '+' and '−' designate the two polarization states for an asymmetry experiment. B_t is the magnetic holding field at the target.*

	Tensor ($B_t \gg 11.7$ mT)		Vector ($B_t \gg 11.7$ mT)		Vector ($B_t \ll 11.7$ mT)	
	+	−	+	−	+	−
States after 1st sext.	1 , 2 , 3		1 , 2 , 3		1 , 2 , 3	
MFT	$1 \leftrightarrow 4$		$3 \leftrightarrow 4$		$3 \leftrightarrow 4$	
States after MFT	2 , 3 , 4		1 , 2 , 4		1 , 2 , 4	
States after 2nd sext.	2 , 3		1 , 2		1 , 2	
SFT	$2 \leftrightarrow 6$	$3 \leftrightarrow 5$	$2 \leftrightarrow 6$	off	$2 \leftrightarrow 6$	
States after SFT	3 , 6	2 , 5	1 , 6	1 , 2	1 , 6	
WFT	off		off	$1,2 \leftrightarrow 3,4$	off	$1,6 \leftrightarrow 5,4$
States after WFT	3 , 6	2 , 5	1 , 6	3 , 4	1 , 6	4 , 5
Tensor Polariz. P_{zz}	+1	−2	+1	+1	+1/2	+1/2
Vector Polariz. P_z	0	0	+1	−1	+5/6	−5/6
Figure of merit	18		8		5.6	

3.4.3 Principle of RF transitions

The mechanism of RF induced transitions between hyperfine states is well known and has been discussed in several publications (see for example Ref. [102, 103, 104, 105]). Here, the discussion is restricted to some aspects relevant for the design of deuterium RF transition units for our experiment.

With the introduction of an oscillating magnetic field, transitions between two selected energy substates can be induced, provided that the frequency of the RF field matches with the energy splitting of the two substates in the static field. In the case of an atomic beam, a gradient is superimposed on the static field in order to ensure that the resonance condition is met exactly once for each atom passing through the RF field. The hamiltonian takes the form

$$H = H_{stat} + H_{RF}, \qquad (3.34)$$

where the additional term

$$H_{RF}(t) = \mu_B(g_I \, \vec{I} + g_J \, \vec{J}) \cdot \vec{B}_{RF}(z(t)) \cos(2\pi\nu \, t) \qquad (3.35)$$

describes the interaction of the spins with the oscillating field (ν = radio frequency, $B_{RF}(z(t))$ = RF field amplitude along the trajectory $z(t)$). The 'strength' of the transition between the substates can be characterized by the corresponding transition matrix element $\langle k \mid H_{RF} \mid \ell \rangle$ whose values are shown as a function of magnetic field strength in Fig. 3.14.

An RF transition is called either a *sigma* (σ) or *pi* (π) transition depending whether the oscillating field has to be parallel or perpendicular to the static field in order to obtain a nonzero interaction matrix element. σ-transitions correspond to $\Delta m_F = 0$, π-transitions to $\Delta m_F = \pm 1$. For deuterium the only σ-transitions are the 3-5 and 2-6 transitions.

Conventionally, RF units are classified according to the regime in which they operate and to the states that are involved in the transition. A transition unit that operates in the weak field limit, and which only induces transitions within a multiplet ($\Delta F = 0$), is called a weak field transition (WFT). Typical frequencies of the RF field are 5-15 MHz (corresponding to $B \simeq 0.5 - 1.8$ mT). In a simplified picture, a WFT reverses the populations of states with opposite m_F within the same multiplet. For example in a so-called 1-4 WFT, the transitions 1-2, 2-3 and 3-4 happen at the same static field for a given radio frequency. However, a full description shows that the different transitions involved in the process will be encountered in a sequence which depends on the amplitude and sign of the static field gradient (see ref. [102]). As Fig. 3.15a shows, this effect can be enhanced by going to an intermediate field (generally 2-3 mT) with appropriate field slope, so to *spatially* separate the different resonances typically by a few cm. By then restricting the RF field around some of the resonances, one can induce selected transitions (e.g. 2-4, or 3-4). This type of transition is called a medium field transition (MFT). Finally, the transitions between states belonging to different multiplets ($\Delta F = \pm 1$) are called strong field transitions (SFT), though the static field is typically smaller or of the same order as the critical field. As Fig. 3.15b shows the strong field transitions are well separated at frequencies above 350 MHz and various transitions can be made within the same transition unit by varying the magnetic field strength.

Next, we wrote a computer code to simulate RF transitions by numerically solving the time-dependent Schrödinger equation. With this code extensive calculations were performed for both the MFT and SFT to study various transitions at different configurations.

For example, calculations were performed for the SFT using the following procedure. All the initial occupation numbers n_k's of hyperfine states $|k\rangle$ are set to the configuration under study, namely, $n_1 = n_2 = n_3 = 1/3$ and $n_4 = n_5 = n_6 = 0$. We then compute the transition by iterating the Schrödinger equation

$$i\hbar \frac{d}{dt}|\psi\rangle = H(t)|\psi\rangle = \Big(H_{stat}(t) + H_{RF}(t)\Big)|\psi\rangle \; . \tag{3.36}$$
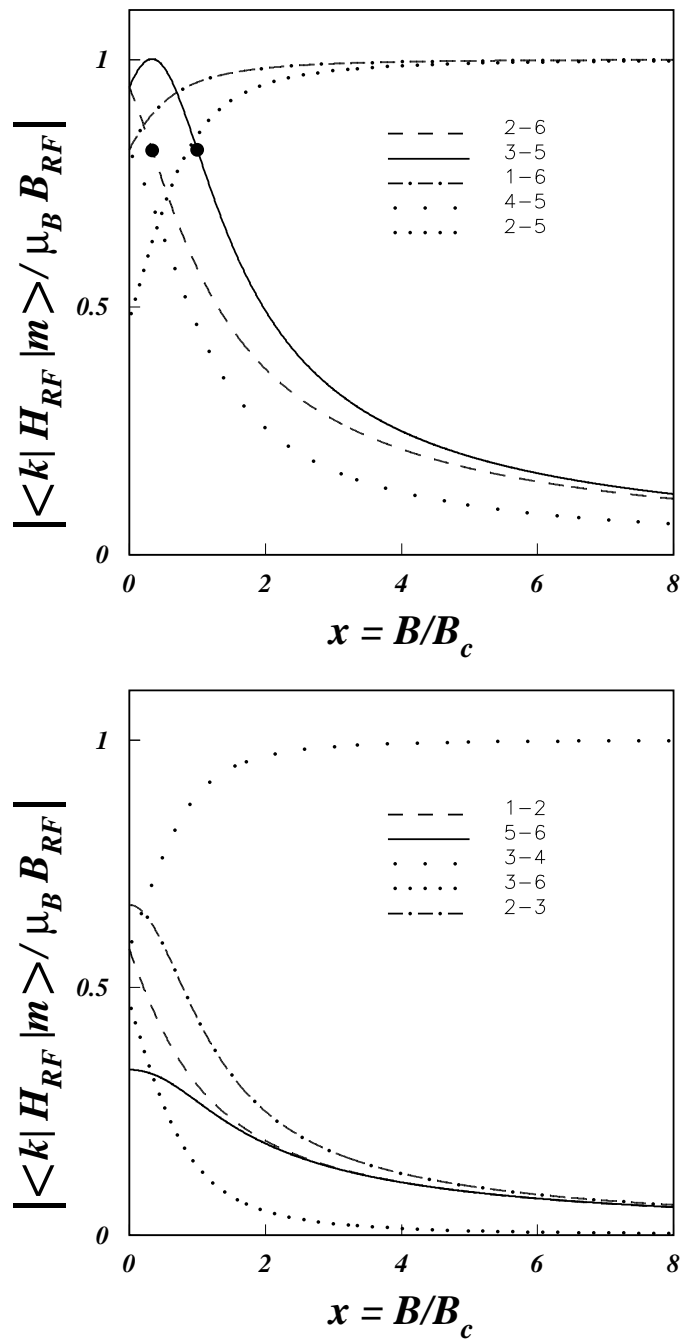
Figure 3.14: *RF transition matrix elements of deuterium as a function of the reduced static field. All possible single-photon transitions are shown. The two dots show the field strength at which our SFT (2-6 and 3-5) operates.*
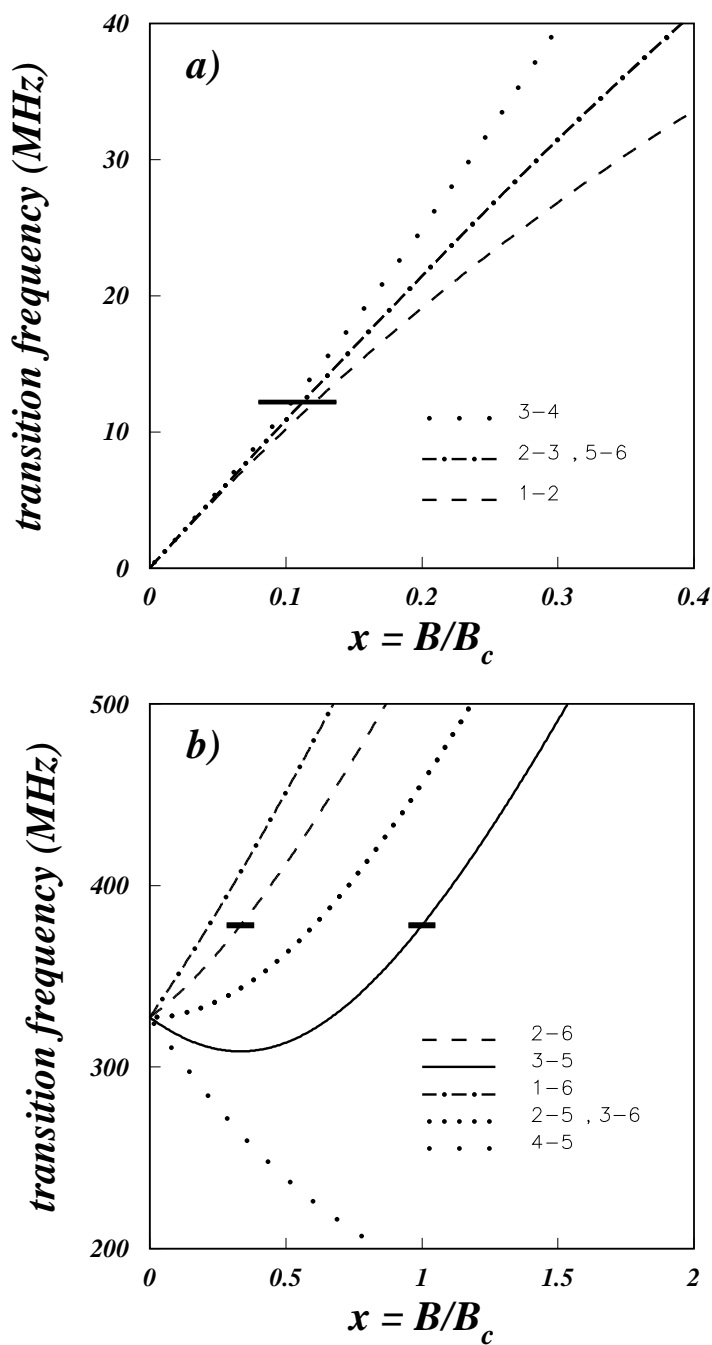
Figure 3.15: *Resonance frequencies of the deuterium hyperfine transitions as a function of the reduced static field. The thick segments show the regions in which our RF units operate. (a) 1-4 WFT. (b) 2-6 and 3-5 SFT.*
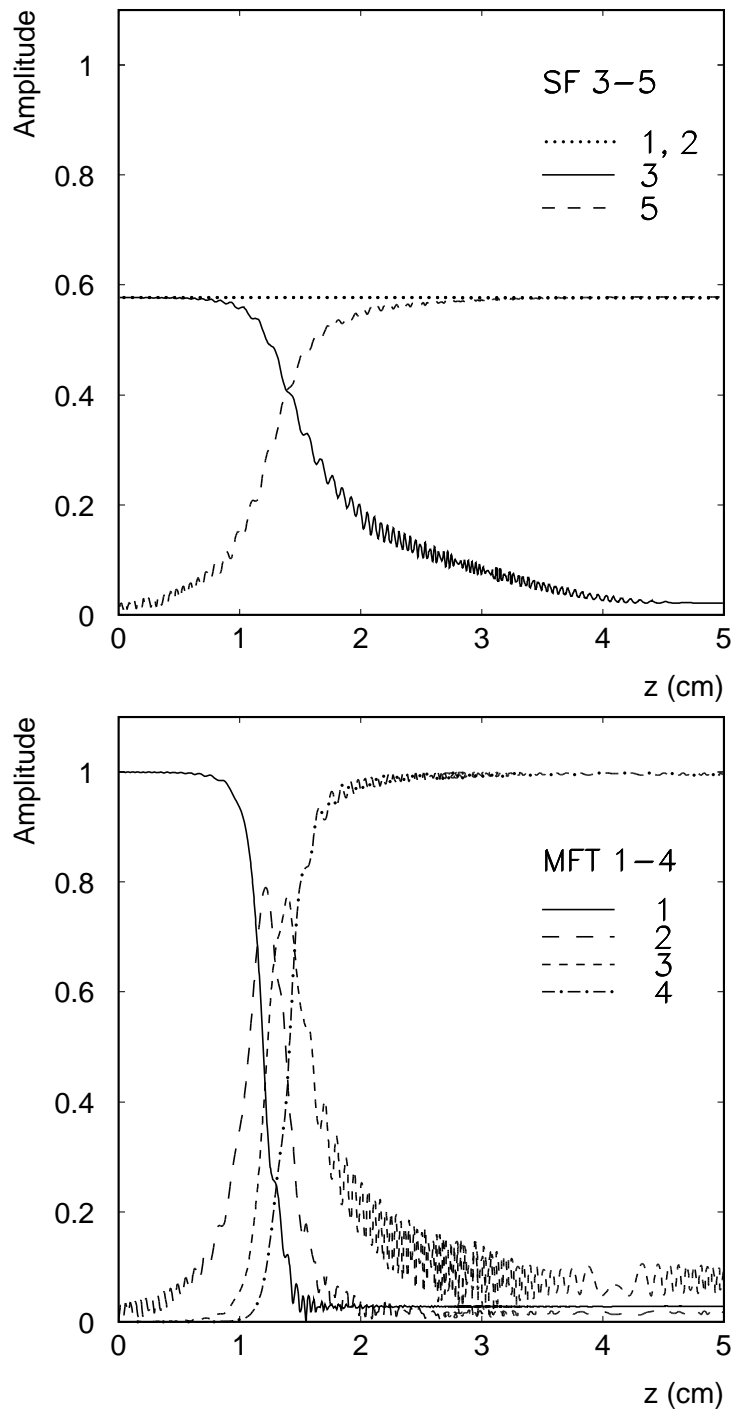
Figure 3.16: *Population amplitudes of deuterium atoms in the RF transition units calculated with the simulation codes described in the text. Top: SFT 3-5 transition (for atoms initially with an equal population of hyperfine states 1, 2 and 3). Bottom: MFT 1-4 transition (for atoms initially restricted to hyperfine state 1).*

$|\psi\rangle$ is expressed in the basis $|k\rangle$ of H_{stat} as

$$|\psi\rangle = \sum_k c_k(t)|k\rangle, \tag{3.37}$$

where the expansion coefficients $c_k(t)$ are the time-dependent probability amplitudes to be solved. This basis is updated after each iteration according to expression 3.26 taking into account the small change of the static field experienced by the moving atom. By definition, the population of a hyperfine state is $n_k(t) = |c_k(t)|^2$. The computation starts at $z_{in} = 0$ cm and ends at $z_{out} = 5$ cm. The RF field amplitude $B_{RF}(z)$ is taken to be Gaussian distributed along the path z inside the unit and rapidly decreases outside this region. The direction of the RF field is chosen to be parallel to that of the static field $B(z)$ so that the requirement of a σ-transition is satisfied. The static field follows a straight line of given slope $dB/dz = 0.1$ mT/cm (the sign of the slope turns out to be irrelevant), while the central value $B_0 = B(z \sim 2.5$ cm$)$ of the static field is set such as to satisfy the resonance condition for the examined transitions ($B_0 = 3.9$ mT for 2-6 and $B_0 = 11.69$ mT for 3-5) at the chosen radio frequency $\nu = 378$ MHz. The calculated efficiency of the transition, ε, is then defined as the final occupation $n_5(z_{out})$.

Fig. 3.16 (top) shows the results of such a calculation for the SFT 3-5 transition with a 0.05 mT maximum RF field amplitude. It is seen that both hyperfine states 1 and 2 are unaffected, while ε_{3-5} is almost 100% within the given 5 cm distance of the SFT unit. Similar calculations for the MFT 1-4 transition are shown in Fig. 3.16 (bottom). Here, the calculation assumes that the atoms are initially only in hyperfine state 1, and the RF field direction is chosen along the z-axis with a maximum amplitude of 0.05 mT and a frequency of 10 MHz. The $B(z)$ is chosen to have a central value of 0.8 mT and a slope 0.14 mT/cm. It can be seen that the 1-4 transition is actually performed by three consecutive transitions, 1-2, 2-3 and 3-4, such that overall the transition behaves like a 1-4 transition and the states 2 and 3 are not affected.

3.4.4   Principle of polarimetry

In an internal target experiment a source delivers polarized particles into a window-less conductance limiter through which the circulating beam passes. Target depolarization mechanisms originate from the limitations of the source of polarized particles, the storage-cell environment, and beam-induced depolarization effects. Thus, it is imperative to develop reliable, fast and accurate polarimetry methods to monitor the target polarization.

The polarization of the injected atoms will be less than 100% due to inefficiencies of the polarizing devices. In addition, due to non-unity of the degree of dissociation, there will be molecules injected into the storage cell. These molecules are unpolarized and will dilute the target polarization. Furthermore, the storage cell will receive a contribution from

unpolarized background gas, mainly molecules from the ABS and the target chamber. Additional polarization losses can originate from the finite magnetic holding field applied over the storage cell, the magnetic fields induced by the circulating beam bunches [106], and from spin-exchange collisions [107]. Finally, the interaction with the cell walls can be an important source of depolarization inside the storage cell [108, 109]. Such losses are suppressed by using suitable wall coatings and it has been demonstrated that Teflon-coated cells are comparably better than cells of bare aluminum [109]. If such cell coatings are used, then the stability of the coating, e.g. against radiation damage in an electron storage ring, has to be understood.

We consider two polarimetry schemes here. One of the methods, the corresponding apparatus is called the Rabi polarimeter, is based on sampling the target gas and relies on the hyperfine coupling in order to infer the nuclear polarization. As was shown in Fig. 3.13, polarized atoms will be either focused or rejected when they pass through a sextupole magnet. Therefore, by placing a sextupole magnet and consequently analyzing the intensity of the sampled atoms, one can obtain information on the nuclear polarization of the sampled gas[3].

The other method is based on the analysis of ions which were extracted from a storage cell placed in an electron storage ring. This ion-extraction method takes advantage of the ionization of atoms and molecules by the electron beam passing through the target cell. The number of ions produced along the storage cell is directly proportional to the local target density and the beam current. The polarization measurement samples the target in exactly the same manner as the nuclear or particle physics experiment under consideration. Furthermore, by uniformly extracting these ions from the cell, measuring their atomic and molecular fractions, and by directly determining their nuclear polarization, one can obtain the effective target polarization *independent* of its spatial and temporal variations.

This can be seen as follows. The average target polarization can be expressed in our polarimetry experiment by

$$\langle\langle P \rangle\rangle_{\text{pol}} = \int I_e(z)\rho_D(z)P_{zz}(z)\,dz, \tag{3.38}$$

while in our scattering experiment we have

$$\langle\langle P \rangle\rangle_{\text{asym}} = \int I_e\rho_D(z)P_{zz}(z)\sigma(z)S(z)\,dz. \tag{3.39}$$

Here $\sigma(z)$ is the cross section of the reaction and $S(z)$ the phase space of the detection system. The double brackets denote the experimental measured values. In our scattering

---

[3]In the HERMES experiment [25] a more elaborate scheme is used consisting of permanent sextupole magnets and RF transition units.

experiment, $\sigma(z)$ and $S(z)$ all have little dependence on the target z-position which allows that they can be factorized from the integral. Therefore, the measured asymmetry in our scattering experiment can be expressed by

$$
\begin{aligned}
\langle\langle A\rangle\rangle_{\text{asym}} &= \frac{\displaystyle\int I_e\rho_D(z)P_{zz}(z)\sigma(z)S(z)A(z)\,dz}{\langle\langle P\rangle\rangle_{\text{asym}}} \\
&= \frac{\displaystyle\int I_e\rho_D(z)P_{zz}(z)\sigma(z)S(z)A(z)\,dz}{\langle\langle P\rangle\rangle_{\text{pol}} \,\cdot\, \displaystyle\int \sigma(z)S(z)\,dz}.
\end{aligned}
\tag{3.40}
$$

One sees that in this case a measurement of the total target polarization $\langle\langle P\rangle\rangle_{\text{pol}}$ is sufficient. Only in case of a strong z-dependence in $\sigma(z)$ and/or $S(z)$, Eq. 3.40 starts to break down. Then, one would need to measure the 'differential' target polarization $P_{zz}(z)$. For our experiment the function $\sigma(z)S(z)$ is only slightly z-dependent (see Fig. 3.4, 6.10 and 6.13).

When performing an electron scattering experiment with a polarized internal target, a small fraction of the target gas in the storage cell is ionized. At the electron energy of 565 MeV used in our experiment, the ionization cross section for deuterium atoms amounts to 1.3×10^{-19} cm^2 [110, 111]. Therefore, a sufficient number of ions can be extracted from the cell (up to 75 nA in the present experiment) which allows for an accurate mass and polarization analysis within a reasonable amount of time (minutes). The interaction time of a high-energy electron with an atom is in the order of 3×10^{-19} s, sufficiently fast that the nuclear polarization is preserved [112] in the ionization process. The momentum transfer during ionization is small, so that the transverse momenta of the ions are dominated by thermal motion. By applying a strong longitudinal magnetic field, these ions can be confined and extracted from the storage cell. This magnetic field not only provides the trapping force for the ions, but also defines the target spin and polarization. Note that for a continuous-wave electron beam, the space charge of the electrons provides an additional confining force for the ions.

Fig. 3.17 schematically shows the axial ion-extraction system and the electrostatic field distribution for this cylindrical lens configuration. On one side of the storage cell, ions are repelled by a lens at a positive voltage (+100 V with respect to the cell). On the other side, ions are extracted and accelerated using three consecutive lenses. A longitudinal 30 mT magnetic field is applied over the cell region in order to prevent the ions from hitting the cell walls. The simulation code SIMION [113] was used for the geometrical and electrostatic design of the lenses. Calculated trajectories are shown for low-energy ions ($\sim$0.3 eV) with an arbitrary angle and position on the central axis of the cell. For optimal ion extraction, the voltages on the three extraction lenses are $V_{EL_1}=-200$ V, $V_{EL_2}=-800$ V, and $V_{EL_3}=-2500$ V. It is clearly seen that the extracted ion beam can be transported downstream for subsequent polarization analysis.
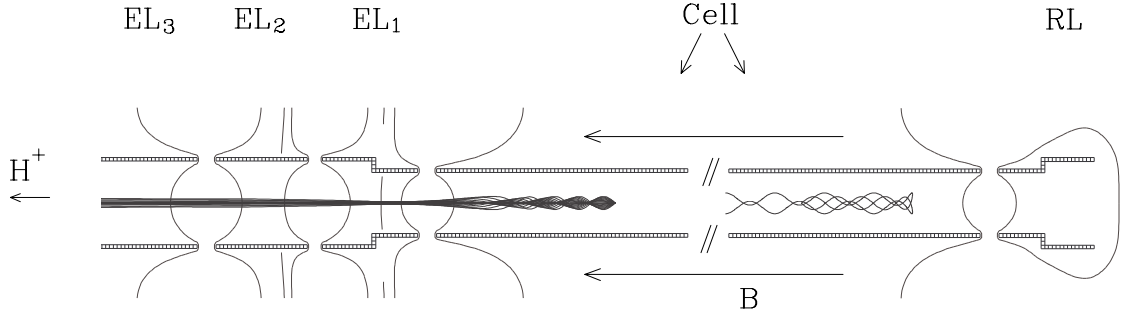
Figure 3.17: *Ion extraction from a storage cell using cylindrical lenses. The equipotential curves and the ion trajectories were calculated with SIMION. RL corresponds to a repeller lens, while EL_{1-3} constitute a triplet of extraction lenses. Note that the storage cell has a 15 mm diameter and a 400 mm length.*

Once the ions are extracted, they can be accelerated to an energy suitable for an appropriate polarimetry reaction. To measure deuteron tensor polarization, the reaction $^3\mathrm{H}(\overleftrightarrow{d},\mathrm{n})\alpha$ can be employed. Here, the neutron angular distribution is related to P_{zz} and is given by

$$n(\theta) \propto 1 - \frac{f}{4} P_{zz}(3\cos^2\theta - 1), \tag{3.41}$$

where θ is the angle of the outgoing neutron with respect to the deuteron spin direction, and $f = 0.959 \pm 0.006$ for 51 keV deuteron energy [114].

For hydrogen and deuterium targets, it is essential to determine the atomic fraction ξ, since the molecules provide a background which in general dilutes the target polarization. Hence, a mass analyzer is needed. For example, an $\mathbf{E} \times \mathbf{B}$ velocity filter, a so-called Wien filter, can be employed. In case of unpolarized molecules, the total polarization of the target species can be expressed as

$$P_{zz}^{\mathrm{tot}} = \frac{n_{\mathrm{D}}}{n_{\mathrm{D}} + 2n_{\mathrm{D}_2}} P_{zz}(\mathrm{D}^+) = \xi P_{zz}(\mathrm{D}^+), \tag{3.42}$$

where n represents the target density and $P_{zz}(\mathrm{D}^+)$ the tensor polarization of the D^+ ions.

In summary, all the considerations discussed here were essential for the design of our target. In the next chapter we will show the setup that was realized for our experiment.